Large-scale troughs on Asteroid 4 Vesta accommodate opening-mode displacement

Hiu Ching Jupiter Cheng[1] and Christian Klimczak[1]

[1]Structural Geology and Geomechanics Group, Department of Geology, University of Georgia, Athens, GA 30602, USA

Key Points:

- Trough morphology is inconsistent with the previously proposed fault origin and points to an opening-mode fracture origin.
- Normal faulting is not expected to be initiated above ~3–55 km in Vesta's lithosphere.
- Opening displacements from jointing contributed to the topographic expressions of large-scale troughs.

Abstract

Asteroid 4 Vesta hosts two sets of enormous troughs, Divalia Fossae that encircle two-thirds of the equator and Saturnalia Fossae located in the northern hemisphere. These troughs were interpreted as grabens, thus invoking faulting. The trough sizes, their linear arrangement, and overall morphology leave no doubt that their origin is tectonic, but structures other than faults have not been considered. To test if they are fault-related or formed by accommodating opening-mode displacement (i.e., jointing) without subsequent shear, we investigate the map patterns, cross-sectional geometries, and variations of relief and width along the trough lengths. Relief and width could relate to the vertical displacement of faults and aperture of joints, respectively, and they therefore reveal differences in fracturing behavior. We analyzed six major troughs on Vesta, four

This article has been accepted for publication and undergone full peer review but has not been through the copyediting, typesetting, pagination and proofreading process, which may lead to differences between this version and the Version of Record. Please cite this article as doi: 10.1029/2021JE007130.

belonging to Divalia Fossae, and two to Saturnalia Fossae. No map patterns are diagnostic of faulting or jointing. For each pair of trough-bounding scarps, the maximum relief does not lie at the trough center, and the two maxima occur at different positions along the trough. In contrast, troughs are widest near the centers of the troughs. These characteristics are inconsistent with graben formation but are consistent with jointing. Furthermore, rock-mechanical calculations that account for Vesta's low gravitational acceleration and degree of fracturing reveal that faulting is not favored to be initiated at depths above at least ~3 but as much as 55 km within Vesta's lithosphere. Therefore, jointing or mixed-mode fracturing, both involving opening-mode displacements, are more plausible fracturing mechanisms for the Divalia Fossae.

Plain Language Summary

The camera on the Dawn spacecraft captured two sets of large linear depressions, or troughs, on asteroid Vesta. Previous studies hypothesized that these troughs are fault-bounded valleys with a distinct scarp on each side that together mark the downward drop (sliding) of a block of rock. However, cracking of rock can also form troughs, an origin that has not been considered before. Structures formed by sliding and cracking form different map patterns, have different morphologic expressions, and are controlled by different stresses acting on the rock volume. Although trough shape does not display any diagnostic map patterns, the morphology of the troughs is consistent with cracking because troughs are widest at the middle and narrow towards both ends. Calculated stresses are not favorable for sliding to be triggered within the uppermost ~3 to 55 km of Vesta's rock volume, but instead, the physics shows that rocks there are favored to crack apart. Therefore, the formation of these troughs must involve the opening of cracks, which is also important for understanding landforms on other small planetary bodies elsewhere in the Solar System.

Keywords: planetary tectonics, Vesta, opening-mode fracture, lithospheric strength of Vesta

1. Introduction

1.1. Vesta's tectonics

The Dawn mission (Russell and Raymond, 2011) explored Asteroid 4 Vesta and revealed the presence of two sets of large-scale linear structures (Figure 1). The Divalia Fossae vary in width from several hundreds of meters to up to ~20.5 km, are bounded by steep scarps, and encircle approximately two-thirds of the asteroid. The Saturnalia Fossae are oriented northwest–southeast and differ in orientation from the Divalia Fossae by ~30°. Saturnalia Fossae are exposed only in the northern hemisphere, and their southern extent is truncated by the Divalia Fossae. Photomosaics and the digital terrain model derived from Dawn Framing Camera (FC) images (Sierks et al., 2011) allow for detailed mapping and structural analysis of these troughs.

Previous work found that the Divalia and Saturnalia Fossae are concentric around the Rheasilvia and Veneneia basin centers, respectively (Figure 1), which was interpreted as evidence that trough formation was directly triggered by impacts (Jaumann et al., 2012). The impactor-origin has been the leading hypothesis for the formation of the Davila Fossae and thus it serves as a geologic constraint for establishing global stratigraphy (e.g., Schäfer et al., 2014; Williams et al., 2014; Yingst et al., 2014) and numerical studies (e.g., Bowling et al., 2014; Stickle et al., 2015) of Vesta. However, recent work identified the Divalia Fossae to clearly crosscut the Rheasilvia basin, and the Divalia Fossae to have no spatial relationship with the center of the Rheasilvia basin (Cheng and Klimczak., 2022). Although the established crater statistics in Cheng et al. (2021) neither confirm nor refute the simultaneous formation of the Divalia Fossae and Rheasilvia Basin, their large uncertainties allow for the Divalia Fossae to have formed long before or after the

Rheasilvia impact (Cheng et al., 2021). Taking together the established age relationships and the crosscutting relationships between troughs and basin, it is plausible for the Divalia Fossae to have formed as a long-term consequence of the Rheasilvia impact (Cheng and Klimczak., 2022), perhaps tied to changes in orientation or rotation of the asteroid (Mao and McKinnon., 2020; Karimi and Dombard, 2016). This newly proposed formation hypothesis contradicts with the leading hypothesis of the impact directly triggering the troughs, and is yet to be tested and serve as a geologic constraint by other research.

Divalia Fossae are observed to be flat-floored and interpreted as grabens formed by normal faulting, with vertical displacements in excess of 5 km (Buczkowski et al. 2012). Subsequently, multiple studies have interpreted Divalia Fossa and similar troughs on Vesta as grabens, half-grabens, and horst-graben structures (Ruesch et al., 2014; Schäfer et al., 2014; Scully et al., 2014; Yingst et al., 2014). Several modeling studies have considered the specific tectonic causes for the faulting. They have used numerical modeling to simulate the amount of deformation associated with the formation of the Rheasilvia basin (Bowling et al., 2013). They have also combined laboratory and numerical experiments to model subsurface failure as a consequence of oblique impacts into a spherical target (Stickle et al., 2015).

No alternative types of tectonic landforms and corresponding structures, such as different fracture types (e.g., opening-mode or mixed-mode fractures) or other origins (e.g., the collapse caused by perhaps some compositional layering or dike intrusion), have been proposed for the troughs on Vesta, so far. Since each set of troughs formed along a structural trend (i.e., an east–west orientation for all troughs as part of Divalia Fossae) with their origin linked to the large impact basins (i.e., Rheasilvia and Veneneia; Jaumann et al., (2012)) or spinning of the asteroid (Karimi and Dombard, 2016; Mao and McKinnon, 2020; Cheng and Klimczak., 2022), it is plausible that the troughs have a tectonic origin. In particular, opening-mode fracturing through jointing and diking is an ubiquitous fracturing process in the upper portion of the Earth's lithosphere, but it is unknown to what extent these processes played a role in the formation of Vesta's troughs. Furthermore, the rheologic structure and depth of the brittle portion of Vesta's lithosphere and its influence on the formation of tectonic structures have not been evaluated. In this study, we specifically test if the troughs could have been formed by opening-mode fracturing in the form of jointing. To achieve that, we collect geologic observations that distinguish between faulting and jointing, and we assess the potential for faulting and jointing from a rock mechanical standpoint. Because faulting and jointing are each forms of brittle deformation, rock-mechanical assessments require characterizing the rheologic structure and the depth of the brittle lithosphere on the asteroid.

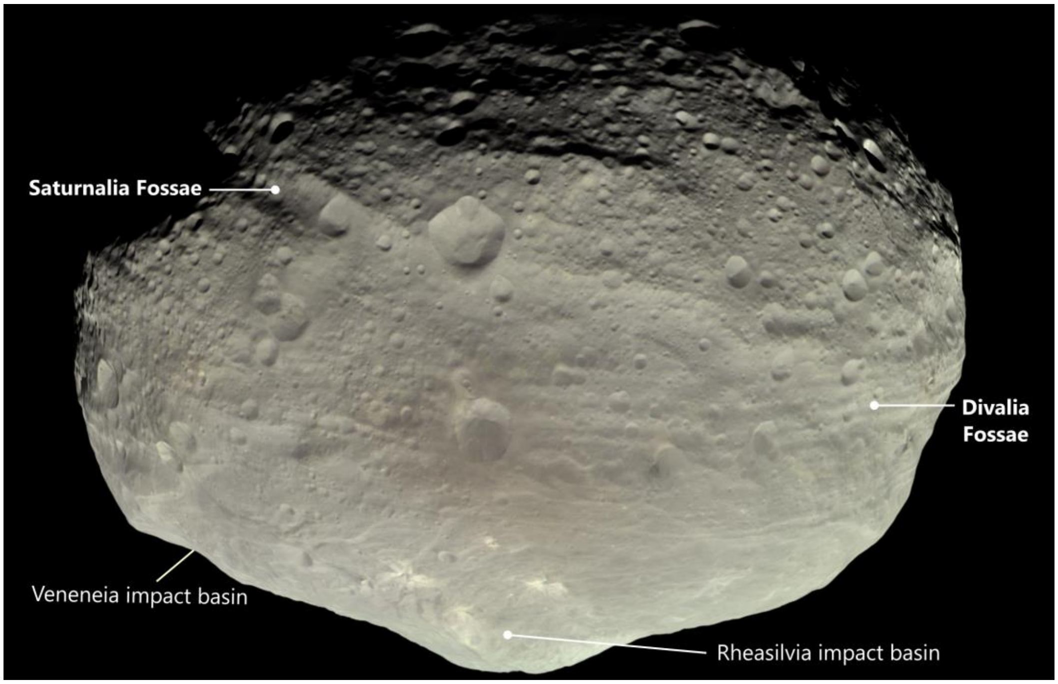

Figure 1. Image of Asteroid 4 Vesta, showing the locations of the Divalia and Saturnalia Fossae, and the Veneneia and Rheasilvia impact basins. The image was captured by the NASA Dawn mission on 24 July 2011 with image processing by Björn Jónsson. <1.5-column figure>

1.2. Normal faulting vs. Jointing

Brittle failure in an extensional tectonic regime, where the overburden pressure represents the maximum principal stress, occurs by opening along joints or slip on normal faults. Joints are planar discontinuities in rock, where fracture walls move perpendicularly apart from one another due to opening displacement (Pollard and Aydin, 1988), and thus they are considered opening-mode fractures along with veins and dikes. In contrast, faulting shows movement parallel to the fault plane and is called sliding-mode or tearing-mode fracturing.

Joints form if tensile stresses reach the tensile strength of the rock in a direction largely perpendicular to the fracture plane. Normal faults form in an entirely compressive stress state via frictional sliding if the hanging wall, the rock mass above the fault plane, slips downward relative to the footwall, the rock mass beneath the fault plane.

In a lithosphere undergoing extension, joints propagate from the surface until they reach a critical depth, where they reactivate as normal faults if the overburden is large enough to shift tensile stresses into the compressive regime (pp. 235–236 in Gudmundsson, 2011). Such fractures possess opening-mode and sliding-mode displacements, and they are known as hybrid or mixed-mode fractures. Mixed-mode fractures are commonly associated with large rift zones on Earth, such as the Almannagjá normal fault at the Reykjaneshryggur–Langjökull rift system of southwest Iceland (Gudmundsson, 1992, 2011), Koa'e fault system associated with the Kīlauea volcano rift zone in Hawaii (Holland et al, 2006), and the Wonji Fault Belt associated with the Ethiopian Rift in East Africa (Acocella et al., 2003). For Earth's gravitational acceleration and its strong basaltic crust, the jointing–faulting transition may be as deep as ~800 meters (Gudmundsson, 2011). With lower gravitational accelerations but given similar rock-mechanical properties, this transition is expected to occur much deeper, and fracture sizes are expected to be much larger in the lithospheres of small bodies, such as moons and asteroids. Hence, opening-mode displacement should be important for structures formed in extensional tectonic regimes on small bodies. Despite this, opening-mode or mixed-mode fractures have not attracted much attention in the planetary community. Establishing the fracturing mode of brittle structures on planetary bodies is important because it dictates interpretations of the stress regime, as well as the kinematics and mechanics of the tectonics responsible for forming the structures.

Structures formed by jointing versus normal faulting can be distinguished by their map patterns, cross-sectional geometries, and displacement profiles, and all have been widely studied in numerous fracturing systems on Earth and other planetary bodies. Normal faults commonly appear as grabens, which are narrow, negative relief structures bounded by oppositely dipping normal faults that create a central down-dropped block (Melosh and Williams Jr, 1989; Schultz et al., 2007; Fossen, 2016). Grabens display a wide range of map patterns, some of which are diagnostic of normal faulting and are found on many different planetary bodies. Grabens commonly have bounding scarps that are straight to arcuate as well as segmented. They may form en échelon patterns and transfer zones between overstepping segments called relay ramps (Peacock and Sanderson, 1994; Crider and Pollard, 1998). Grabens may also involve multiple faulted borders and floors, such as those in complex terrestrial rift systems (Hauber and Kronberg, 2005). In some cases, pit crater chains, which are connected circular depressions that form by the collapse of material into subsurface voids, are aligned with or superimposed on a graben, such as in those in Hawaii (Okubo and Martel., 1998) and on Mars (Wyrick et al., 2004). Normal faults of any kind typically have their point of maximum displacement near the center of the fault, with displacement tapering to zero at the fault tips. This symmetry is well-documented on Earth (e.g., Muraoka and

Kamata, 1983; Dawers et al., 1993; Cartwright et al., 1996), Mars (e.g, Schultz and Lin, 2001; Polit et al., 2009), and the Moon (e.g., Callihan and Klimczak, 2019). Maximum displacements increase linearly with fault length as they grow (Schultz et al., 2006). In cross-section, grabens are typically flat-floored depressions, bounded by two (or more) scarps that face each another.

In contrast, joints can appear in map view as the straight trace of a continuous single crack, or as segmented and discontinuous en échelon traces of small subparallel segments. Although joints can occur as isolated structures, they commonly occur as sets of parallel joints. Closely spaced joints may interact to form hook-shaped linkages (Pollard and Aydin, 1988). Joint displacement, commonly referred to as aperture, reaches its maximum in the center of the structure, tapering out symmetrically toward the tips (Vermilye and Scholz, 1995). In map view, joints may therefore appear as wide troughs that narrow toward the tips. The maximum aperture increases sublinearly with length as joints grow (Olson, 2003). In contrast to a graben, the surface expression of a vertical joint is expected to be shaped as a narrow V in cross-section, but this shape is likely degraded by slope instability, where infilling of collapsed material causes it to become shaped like a wide bowl. Open void spaces within the joint may not be visible at the surface due to collapse of and filling by surficial material.

In this paper, we investigate the map patterns, cross-sectional geometries, and morphological variations of the large-scale troughs in detail to assess whether they display characteristics of opening-mode or sliding-mode fractures. Based on previously published interior constitution and thermal evolution models of the asteroid, and considerations of strengths of fractured basaltic rock masses, we assess the physical conditions for frictional sliding to be triggered within Vesta's lithosphere for a wide range of rock mechanical properties.

2. Trough map patterns

For structural mapping, we use the HAMO-based Dawn FC clear filter image mosaic with an average pixel scale of 60 m/pixel (Roatsch et al., 2015) and the ~93 m/pixel digital terrain model (DTM; Gaskell, 2012). The DTM is based on the shape model of Vesta derived from FC images, and it has a vertical accuracy of ~6 m (Preusker et al., 2014). These datasets were projected using a sphere with a diameter of 255 km and the Claudia Double-Prime system (Li et al., 2012; WGCCRE., 2014). The two large sets of troughs and their related landforms are included in the mapping, as are the bounding scarps and pit crater chains. For structural mapping, we use ESRI's ArcGIS software to create hillshade images with different illumination conditions and draw topographic cross-sections at ~5 km intervals across the troughs. Trough-bounding scarps are defined by a sharp surface break on the topographic profiles, which were traced on the hillshade images. Structures identified as *certain troughs* are mapped where negative linear relief is bounded by two facing scarps. Long depressions with a single bounding scarp are mapped as *inferred troughs*. Troughs of any category were grouped into one structure where multiple troughs were aligned and separated by only one or several impact craters. Pit craters and chains of pit craters are included in our mapping, as they are aligned with the Divalia Fossae (Buczkowski et al., 2012; Jaumann et al., 2012) and because they are commonly associated with grabens on other planetary bodies (Wyrick et al., 2004). They are mapped where there is a series of at least three aligned circular to elliptical, steep-sided depressions that lack diagnostic features for impact craters or volcanic pits, including elevated rims, ejecta deposits, or lava flows.

Previous work mapped 86 trough lineaments of Divalia Fossae and 7 trough lineaments of Saturnalia Fossae (Jaumann et al., 2012; Yingst et al., 2014), but those analyses did not consider that some troughs are parts of the same structure. Based on the mapping criteria, we identified 55 individual trough lineaments comprising 155 bounding scarps as well as 30 pit crater chains (Figure 2). The structural map is included as shapefiles in the supporting information. Of the 55 troughs, 36 are classified as certain and 19 as inferred. Among those, 30 certain and 9 inferred troughs form six main structures, and the other 16 troughs are smaller structures associated with Divalia Fossae. To each trough, we assigned an id number that increases from south to north. The Divalia Fossae consist of closely spaced E−W striking troughs 1 to 4, with lengths of 335−815 km and widths up to 20.5 km. Trough 1 consists of at least three segments that are widely separated by long inferred trough lineaments, whereas troughs 2 to 4 consist of certain trough lineaments superposed by a few impact craters. Troughs 5 and 6 are part of the Saturnalia Fossae with trough 6 being the widest and longest one. The southern ends of the Saturnalia Fossae are truncated by the Divalia Fossae, therefore their full original lengths are not preserved. All troughs are categorized as being isolated, continuous, and subparallel within their own sets (Figure 2).

None of the Vesta structures have map patterns diagnostic of faulting, such as en échelon segmentation, relay ramps, or multiple faulted borders and floors (nested graben). Instead, trough-bounding scarps are consistently scalloped (Figure 3a). The rims are too scalloped or too degraded to be interpreted as normal faults. In contrast, Matronalia Rupes and other scarps that form the rim of the Rheasilvia impact basin, which is thought to have been emplaced at a similar time as Divalia Fossae, appear remarkably fresh. Map patterns diagnostic for jointing, such as hook-shaped linkages and en échelon traces of subparallel openings, are not readily apparent. Degradation and slope instability are therefore inferred to have influenced the surface expression of the troughs.

Consistent with previous studies (Buczkowski et al., 2012; Jaumann et al., 2012), pit crater chains are aligned with the Divalia Fossae (Figure 2 and 3). Generally, pit crater chains are located on the floors of planetary grabens (Wyrick et al., 2004), but none on Vesta occur within a trough, that is, between two bounding scarps. Pit crater chains on Vesta vary widely in their map patterns, and their full number and extent are unclear due to the superposition of impact craters. Only trough 1 shows a direct transition from the trough into a pit crater chain (Figure 3a). This trough narrows and terminates in a pit crater chain, and smaller pits align with the trough farther away from the termination of the trough. One completely preserved pit crater chain has larger pits in the middle and smaller pits at the two ends of the chain (Figure 3b). Following these map observations, the structures possibly represent multiple stages of trough formation where the scalloped edges of the troughs may be coalesced pits forming from collapsed openings and unstable slopes.

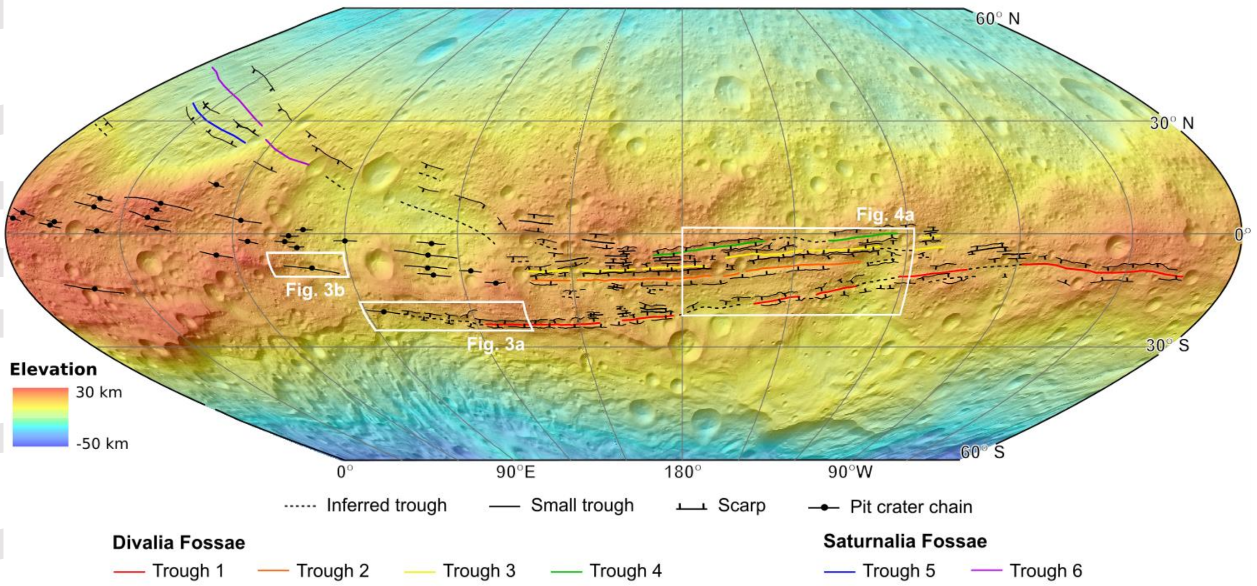

Figure 2. *Digital terrain model of Vesta overlain on hillshade showing a structural map of large-scale troughs and pit crater chains. The map is displayed in sinusoidal projection extending*

between latitudes 60^{o}N to 60^{o}S and longitudes 0^{o} to 30^{o}W. Refer to text for the definition of structural map units. Locations and geographic extents of subsequent maps are indicated by white boxes. The reference elevation is defined to be the mean planetary radius of 262 km. <2 columns, color>

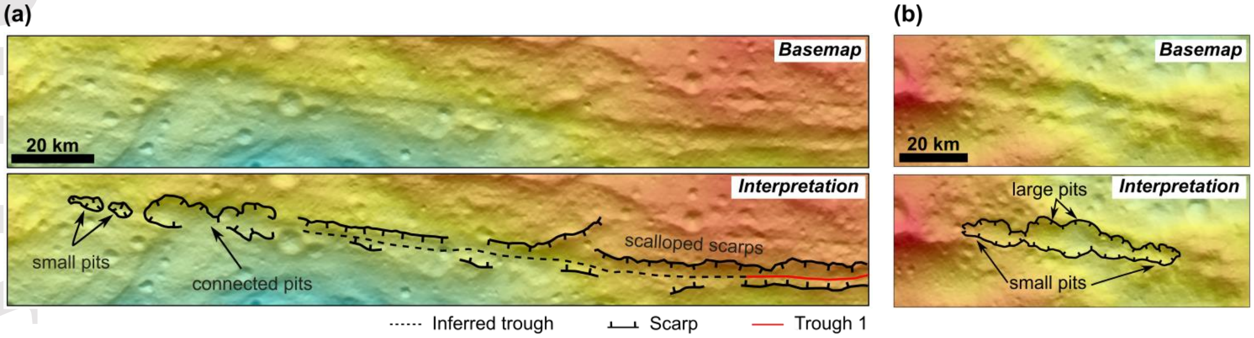

Figure 3. *Base map (top) and structural interpretations (bottom) of scalloped scarps and pits and pit crater chains. (a) Trough 1 terminates into coalesced pits, with smaller pits aligned with and beyond the termination of the trough. (b) A pit-crater chain with larger pits in the middle and smaller pits at the ends. Refer to Figure 2 for the location on Vesta. <2 column, color>*

3. Trough geomorphology

Previous work showed that troughs display a classic flat-floored shape with both walls having a similar slope, which led to their interpretation as grabens (Buczkowski et al., 2012). Based on that interpretation, Buczkowski et al. (2012) measured the topographic differences between the rim and floor of the Divalia and Saturnalia Fossae at several locations and related them to the vertical displacement component of graben-bounding normal faults. Here, we extract and analyze 233 topographic profiles at spacings of 5 km across six large troughs, to examine the cross-sectional geometries, relief, and width variations along the troughs (see supporting information).

3.1. Cross-sectional trough geometries

Cross-sectional shapes for the six troughs were assessed along the 233 extracted profiles. Most profiles contain more than one trough, and 392 individual trough geometries were analyzed. All profiles were examined for topographic changes between the trough rims to identify whether the troughs are flat-floored (no major topographic changes in the center of the trough), or have a different geometry. Trough geometries lacking distinctive rims or superposed by impact craters are classified as inconclusive. One representative profile of the Divalia Fossae has four troughs, with troughs 1, 2, and 3 being bowl-shaped, and trough 4 having a V shape (Figure 4a). Among all assessed topographic profiles, 207 of our 260 conclusive troughs are not flat-floored: 176 are bowl-shaped, and 31 are V-shaped. Only 53 out of 260 conclusive troughs (~20%) are flat-floored; thus, most troughs do not show the cross-sectional geomorphology that is typical for graben. In comparison, Rima Ariadaeus on the Moon (Figure 4b) and grabens and horsts on the northeast flank of Alba Patera on Mars (Figure 4c) have the characteristic flat-floor cross section of landforms caused by normal faulting.

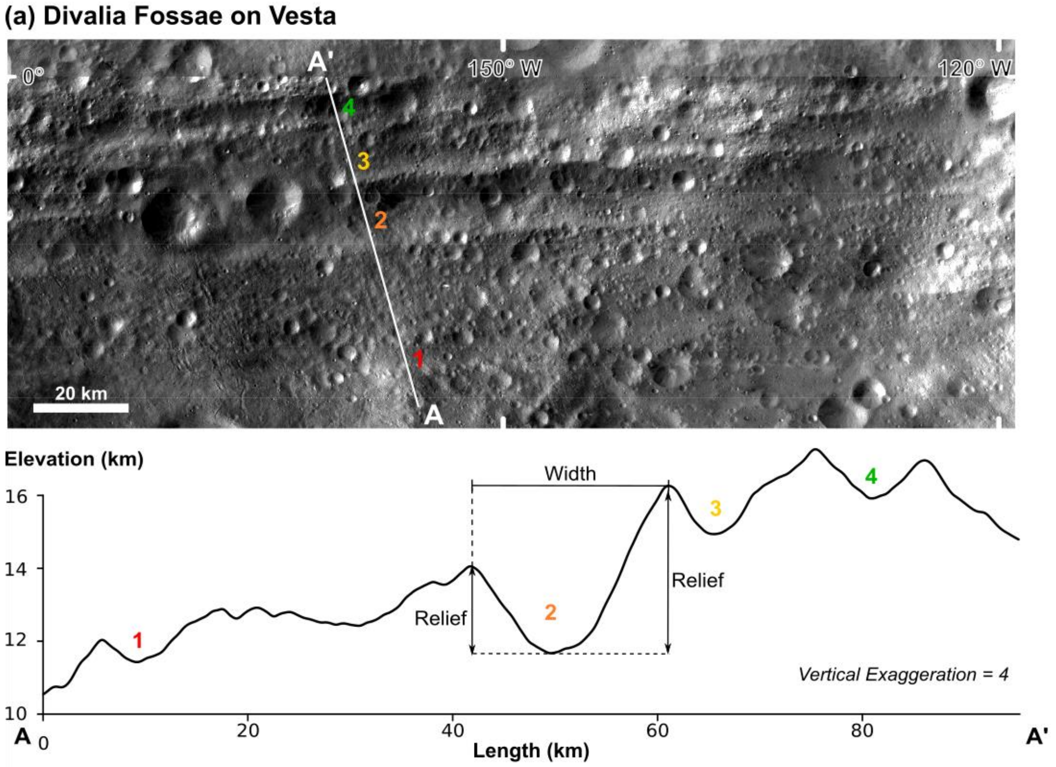
(a) Divalia Fossae on Vesta

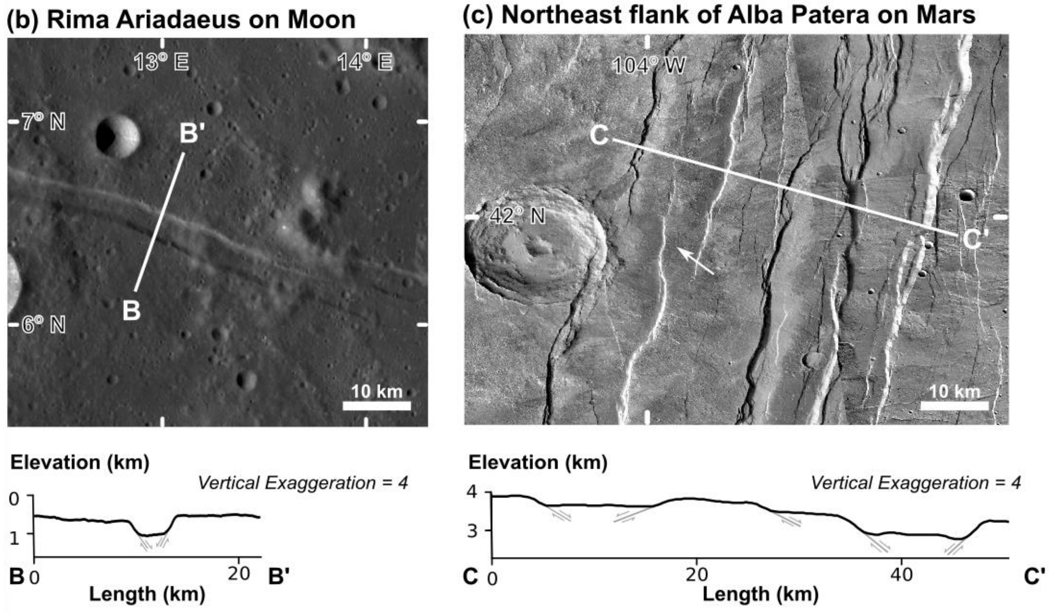
(b) Rima Ariadaeus on Moon

(c) Northeast flank of Alba Patera on Mars

Figure 4. *Typical topographic expressions of troughs on Vesta compared to grabens on the Moon and Mars. The horizontal and vertical scales, and vertical exaggeration are the same for the three topographic profiles. (a) Dawn FC images and topographic profile A–A' of the Divalia Fossae.*

Refer to Figure 2 for the location on Vesta. The profile shows the geometries of four major troughs part of Divalia Fossae. The trough width and relief of two rims are labeled for trough 2. (b) Lunar Reconnaissance Orbiter Camera image (Robinson et al., 2010) with a pixel scale of 73.24 m/pixel and topographic profile B–B' of Rima Ariadaeus on the Moon. The elevation data is based on High-resolution Lunar Topography (SLDEM2015; Barker et al., 2016) with a vertical resolution of ~10 cm and horizontal pixel scale of ~60 m/pixel. An en-echelon stepover is present at the eastern end of the graben. (c) Mars Reconnaissance Orbiter Context Camera (CTX; Malin et al., 2007) image with a pixel scale of ~5 m/pixel and topographic profile C–C' of the northeast flank of Alba Patera on Mars. The elevation data is based on the High-Resolution Stereo Camera of Mars Express (image h0068_0009; Gwinner et al., 2009) with a grid spacing of 125 m, and a vertical accuracy of ~20 m. Normal fault structures are present, including fault segments forming a relay ramp on the western graben (white arrow) and multiple faulted borders at the western rim of the eastern graben. <1.5 column, color>

3.2. Shape variations along troughs

3.2.1. Trough reliefs

Buczkowski et al. (2012) analyzed the topographic differences between the trough floor and rim of Divalia and Saturnalia Fossae and related them to the vertical displacements of faults that form grabens. For comparison, we use the same methodology and expand upon this analysis by assessing six troughs also including Divalia and Saturnalia Fossae but with a denser sampling of the topographic data (supporting information). Structural reliefs for the trough-bounding scarps for each major trough are assessed at 5 km intervals. The shortest trough, trough 5, is 115 km long and includes 24 measurements of relief, whereas the longest trough, trough 1, with a length of 835 km, has 168 measurements of relief. The reliefs of scarps are determined by the maximum elevation differences between the trough floor and rims (Figure 4a). Relief is plotted against the length of map trace, scaled to the total length of the trace, to allow comparison of the two scarps that bound each trough and to test whether maximum relief is at the center of each scarp (Figure 5). If a trough formed as a graben, the maximum vertical displacement of each bounding fault, measured by scarp relief, should lie at the midpoint of the scarp, and maximum vertical displacement should decrease to zero towards each end of the scarp. The shapes of the two profiles per trough, one for each of the trough-bounding scarps, are expected to mimic each other, considering that they lack fault segmentation and linkages. As the southern portion of the Saturnalia Fossae is no longer preserved, the observed maximum relief and its position along the scarp may not reflect the original values, owing to truncation by the Divalia Fossae; nonetheless, we analyze them to investigate if part of the relief profile shows the typical characteristics of faults.

Each pair of relief profiles for the six troughs show that their points of maximum relief are at different positions along trough (Figure 5). Trough 1 is separated into three segments by long muted troughs far from each other, which makes it difficult to determine if they belong to a single structure or multiple structures; the maximum reliefs are marked for each of its segments. Trough 1 is 835 km long with maximum reliefs of the northern and southern rims of 4.74 km and 2.78 km. Trough 2, Divalia Fossa, is 400 km long with corresponding maximum reliefs of 5.73 km and 2.96 km. The northern rim of Trough 2 has the largest relief among the Divalia Fossae, consistent with Buczkowski et al. (2012). Trough 3 is 495 km long with maximum reliefs of 2.92 km and 2.82 km. Trough 4 is 345 km long with maximum reliefs of 3.22 km and 2.68 km. Among the 8 relief profiles of the Divalia Fossae, only the northern rim of trough 2 and the southern rim of trough 3 have maximum relief near the midpoint of the trough with relief decreasing toward the tips (Figure 5a), whereas the point of maximum relief on the other 6 profiles is not near the midpoint, or the scarps have multiple peaks of relief. The results for Divalia Fossae are also consistent with Buczkowski et al. (2012). The opposing scarps of the four troughs in Divalia Fossae have differing relief distributions (Figure 5a).

For the Saturnalia Fossae, the traceable length of trough 5 is 115 km with the maxima of 1.29 km and 3.99 km on the two scarps, whereas the traceable length of trough 6 is 275 km and its maxima of structural relief are 4.20 km and 6.89 km. Since these troughs are truncated by the Divalia Fossae, the measured changes in relief (Figure 5b) reflect an unknown portion of the original structure. Therefore, the location of maximum relief with respect to the full length of the scarps cannot be known. Nevertheless, the preserved portions of the Saturnalia Fossae show a similar asymmetric pattern to that on the Divalia Fossae, where the point of maximum relief occurs at a different location on the opposing scarps (Figure 5b).

In summary, the point of maximum relief lies in the center of only two of twelve scarps. In addition, none of the opposing scarps for any trough have similar relief profiles, making the variations in trough geomorphology highly non-systematic. These findings are inconsistent with normal faulting and suggest that troughs are not grabens.

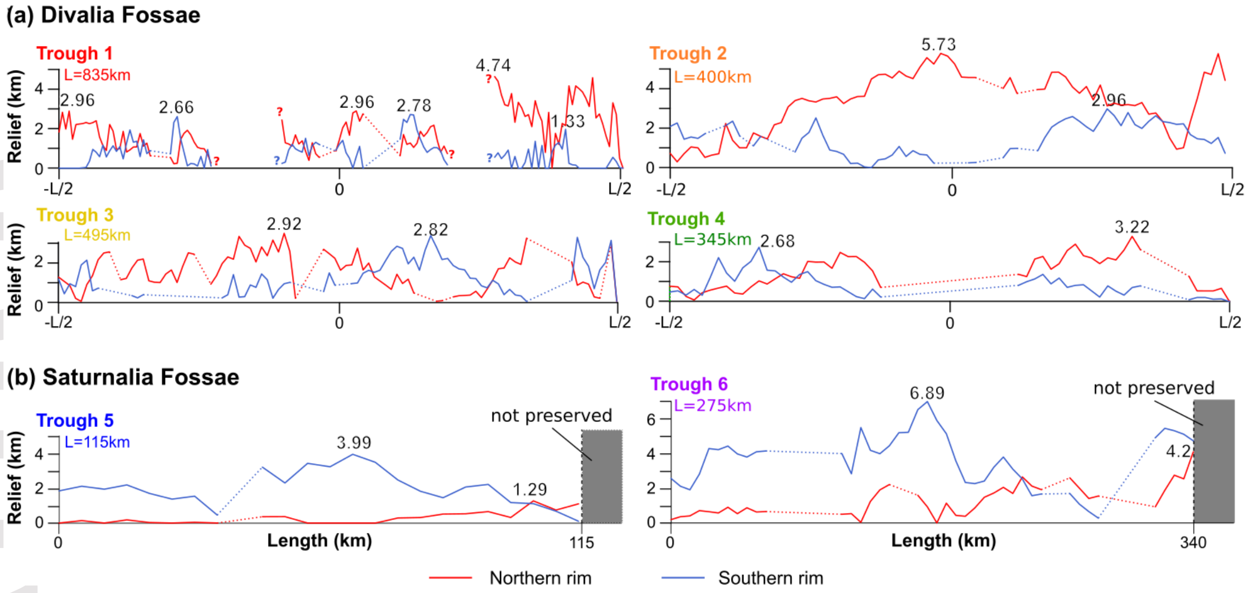

Figure 5. Relief profiles of all analyzed troughs. The reliefs of (a) Divalia Fossae are plotted against distance along the scaled length (L) of the trough. The numerical values of maxima (in km) are labeled at their locations long the trace. Scarps bounding troughs on the north are plotted in red, and southern scarps are plotted in blue. Note that the southern extent of the Saturnalia Fossae (b) is truncated by the Divalia Fossae, and thus their total length and maximum relief are unknown. Their reliefs are plotted against the traceable length in km. <2 columns, color>

3.2.2. Trough widths

As with faults, opening-mode fractures typically have displacement profiles with centrally located maxima that taper to zero at the fracture tips. As the mode of displacement differs, the aperture is formed perpendicular to the fracture surface and is related to the trough widths. Trough width is defined by the horizontal distance between the elevated portions of the two trough-bounding scarps, and it is measured perpendicular to the trough (Figure 4a). We extract width measurements from the previously extracted topographic sections (supporting information) across each of the previously analyzed troughs and plot them along the length of the trough set from west to east (Figure 6). The relief profiles are analyzed for the location of maxima. These individual profiles are summed to identify the cumulative widths for each of the two trough sets to explore their potential total opening-mode displacement. The cumulative width of one set of joints should display a central maximum that tapers towards both ends of the fracture set. Although this pattern is not present, we note that the centers of the troughs could also be the widest if grabens are bounded by dipping normal faults and maximum displacement is centrally located.

The width profiles for each of the four troughs within the Divalia Fossae and the cumulative width profile show their maxima near the center of the troughs (Figure 6a, 6b). As in the relief analysis, trough 1 (Figure 6a) has three segments, and it is difficult to determine if it is a single structure or multiple structures. Trough 1 generally widens eastward and is widest (20.4 km) near the eastern tip. Troughs 2, 3, and 4 have maximum widths of 20.5 km, 15.8 km, and 17.3 km. Maximum width of troughs 2 to 4 occur at a similar longitudinal position on Vesta, centrally located along the length extent of the trough set (Figure 6a). These maxima are all tend to be to the east of the midpoint of troughs. Cumulative width summed across the strike of the Divalia Fossae shows a ~800 km long profile with a maximum of 60.8 km at the center of the overall length trace, tapering toward the tips (Figure 6b).

For the Saturnalia Fossae, the preserved portions of troughs 5 and 6 have maximum widths of 18.9 and 42.0 km (Figure 6c). The cumulative width profile of the Saturnalia Fossae shows a ~280 km long profile with a maximum of 56.2 km near 110 km, tapering towards the western end while the eastern end is not preserved (Figure 6d). The systematic changes and shapes of the individual and cumulative profiles for both trough sets are consistent with the mechanics of opening-mode fractures, suggesting that troughs formed through opening-mode displacement. Although the width distribution along the troughs is also expected for graben formed by dipping normal faults, the relief distributions (Figure 5) are inconsistent with the vertical displacements of graben-bounding faults. Taken together, the shape variation along the troughs is inconsistent with the displacement profiles of normal faults.

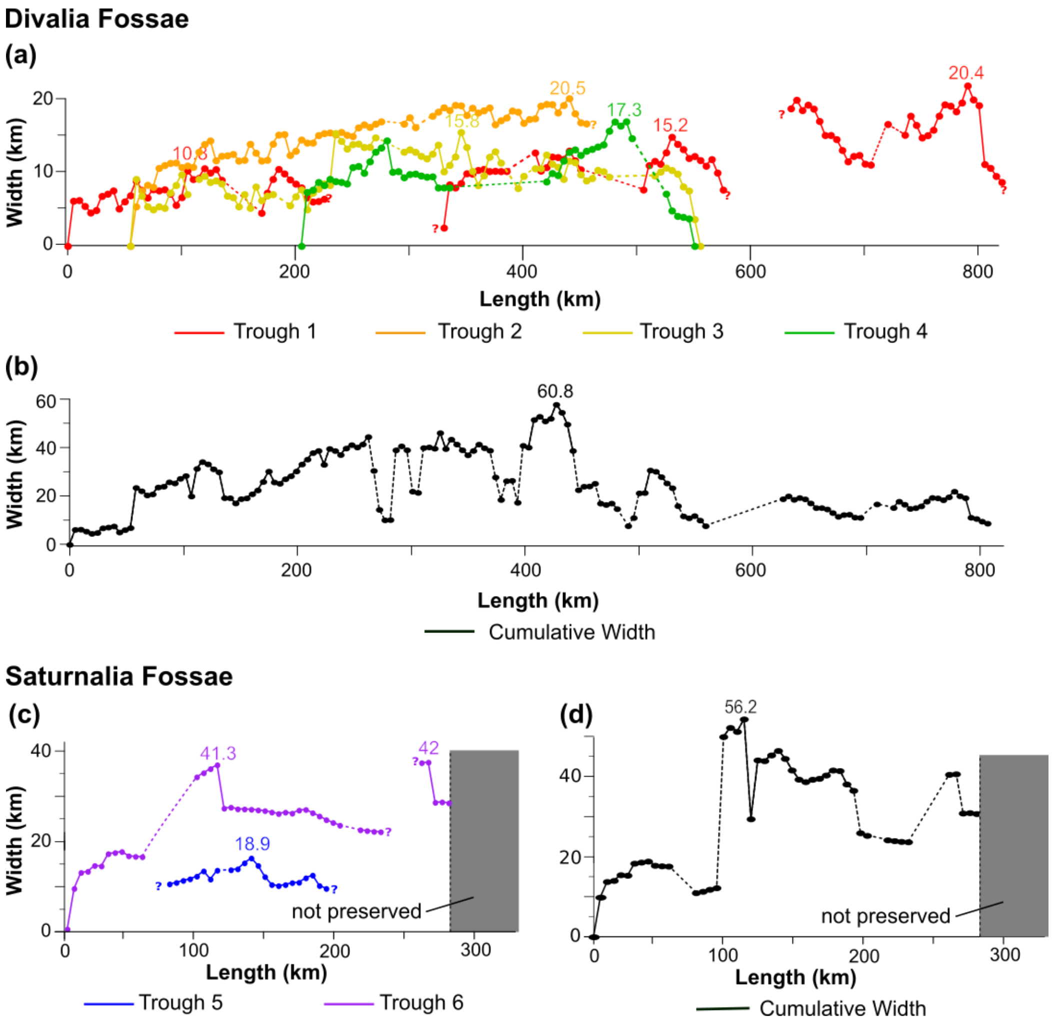

Figure 6. *Width profiles of all analyzed troughs. (a) Individual and (b) cumulative width profiles of the Divalia Fossae of troughs 1 to 4. (c) Individual and (d) cumulative width profiles of the Saturnalia Fossae of trough 5 and 6. The numeric values of width maxima are labeled (in km) at their locations long the trace. Note that the true extent of the Saturnalia Fossae (b) is not preserved and thus the true length and maximum width are unknown. <1.5 column, color>*

4. Lithospheric structure of Vesta

As both faulting and jointing are brittle deformation behaviors, it is important to characterize the strength and depth extent of the brittle portion of the lithosphere, which establishes to what depth brittle failure criteria are appropriate for assessing fracturing behaviors. Since lithospheric strength is influenced by the overburden pressure, which in turn is governed by gravitational acceleration, these parameters must be derived first. Gravitational acceleration is generally assumed to be linear in the upper parts of a planetary body, but for low-gravity objects like Vesta, gravitational acceleration is markedly nonlinear and thus the variation in gravitational acceleration must be considered.

Furthermore, Vesta is a monolithic asteroid that is likely heavily fractured. Such fractured lithospheres are governed by friction between blocks of rock, creating a degree of cohesive strength at the surface of the asteroid. This strength must therefore be considered in assessments of fracture behaviors. For these reasons, we (1) derive the gravitational acceleration and overburden pressure profiles for Vesta, which we use to (2) determine lithospheric strength envelopes. The strength envelopes provide insight to the extent of the brittle portion of the lithosphere, which allows us to specify to what depth brittle failure would have been possible on Vesta. Additional rock-mechanical considerations (3) help us determine at what depths faulting via frictional sliding is the predicted fracturing mode, while accounting for both the nonlinear gravitational acceleration profile and strength of the rock volume.

4.1. Gravitational acceleration and pressure profiles of Vesta

The first step is to derive the gravitational acceleration profile for Vesta can be established from published interior models. Vesta is a differentiated asteroid, and thicknesses, compositions, and densities of core, mantle, and crust have been estimated from geophysical and spectral data collected by the Dawn mission as well as howardite–eucrite–diogenite (HED) meteorites, for which Vesta is widely thought to be the parent body. Vesta has an iron core with a radius of ~108 km and density of ~7850 kg m^{-3} (Ruzicka et al., 1997; Russell et al., 2012; Ermakov et al., 2014), a ~118 km thick (Ermakov et al., 2014) olivine-rich mantle with a density of ~3400 kg m^{-3} (Ruzicka et al., 1997; Zuber et al., 2011; Russell et al., 2012), and a ~36 km thick basaltic crust with a density of 2900 kg m^{-3} (Ruzicka et al., 1997; Zuber et al., 2011; Russell et al., 2012). Using this three-layer model of the interior structure and approximating the shape of the asteroid as a sphere (Figure 6a), the gravity acceleration profile of Vesta can be calculated as:

$$\frac{\delta g}{\delta r} = 4\pi G \rho_r r - 2\frac{g}{r}, \tag{1}$$

where g is gravitational acceleration, r is the radius of the body, G is the gravitational constant, and ρ_r is local material density. The calculated surface gravitational acceleration is 0.26 m/s^2 (Figure 7b), bracketed by the values measured by the Dawn spacecraft, which range from 0.23 to 0.27 m/s^2 (Ermakov et al., 2014). The acceleration due to gravity gradually decreases with depth to the lower mantle at ~120 km, where it then increases until it reaches the core–mantle boundary. From that point, gravitational acceleration drops linearly to zero at the center of the core (Figure 7b), consistent with Stickle et al. (2015).

Next, we utilize our calculated gravitational acceleration profile to assess how overburden pressure, P, changes with depth, z , as given by:

$$P(z) = -\rho_z z g_z. \tag{2}$$

Overburden pressure increases with depth roughly linearly from 0 MPa at the surface to ~120 MPa at the core–mantle boundary, and it increases nonlinearly from there to the core (Figure 7c). This pressure profile is taken as the reference state of stress for the rock-mechanical considerations below.

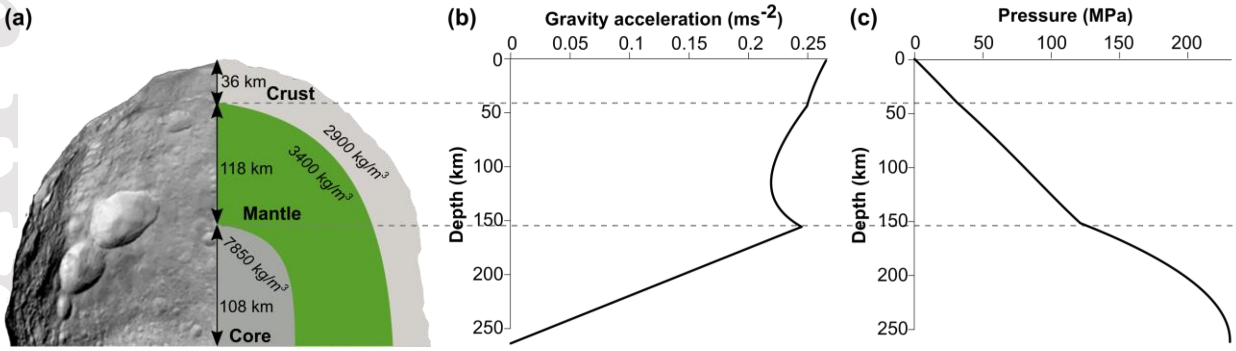

Figure 7. *Gravitational acceleration and pressure profiles calculated using physical parameters of Vesta's interior structure. (a) A three-layer model of Vesta's interior was used to compute depth profiles of gravitational acceleration and pressure. (b) Depth profile of gravitational acceleration. (c) Depth profile of pressure. Dashed lines across the three diagrams indicate crust–mantle and mantle–core boundaries. <2 columns, color>*

4.2. Vesta's lithospheric strength

To explore the type of fracturing involved in the formation of Vesta's large troughs, the extent of the brittle portion of the lithosphere at the time of fracture formation must be established. Overburden pressure plays an important role in defining the lithospheric strength. The thickness of the lithosphere is controlled by the brittle and ductile strength of rock, and rock strength is determined by the weakest rheology at a given depth for a given stress. The upper portion of a solid-surface body with low temperature and confining pressure is controlled by brittle behavior

(Byerlee, 1978) with the strength increasing linearly with depth, independent of the rock type and surface condition (Byerlee, 1978). For all stress calculations, we follow the geologic sign convention where compression is positive. Critical values of the principal stresses for frictional sliding in a dry lithosphere, regardless of its composition, are typically obtained from Byerlee's intermediate- and high-pressure laws (Brace and Kohlstedt, 1980; Kohlstedt and Mackwell, 2010) as:

$$\sigma_1 \cong 5\sigma_3 \qquad \text{for } P < 110\ MPa \tag{3}$$

$$\sigma_1 \cong 3.1\sigma_3 + 210\ MPa \qquad \text{for } P > 110\ MPa, \tag{4}$$

where σ_1 and σ_3 are the maximum and minimum principal stress components with zero pore fluid pressure, respectively. Rock strength in a lithosphere under extension is obtained where the overburden pressure, P, given in Equation (2), is the maximum principal stress (i.e., $P = \sigma_1$). Failure is predicted to occur if the calculated values of σ_3 in Equations (3) or (4) are reached. Rock strength in a lithosphere undergoing shortening is obtained where the overburden pressure is the minimum principal stress (i.e., $P = \sigma_3$), and brittle failure is predicted to occur if the calculated values of σ_1 in Equations (3) or (4) are reached.

In the lower hotter portions of the lithosphere, ductile behavior dominates by several microstructural deformation mechanisms, which are combined under the term *creep*. Here, the strength sharply decreases with increasing temperature and is described by a thermally activated power law (Ranalli and Murphy, 1987; Mackwell et al., 1990; Burov and Diament, 1992):

$$(\sigma_1 - \sigma_3)_d = \sqrt[n]{\frac{\dot{\varepsilon}}{A}}\ \exp(\frac{Q}{nRT}), \tag{5}$$

where $\acute{\varepsilon}$ is the strain rate, A and n are material constants, Q is the activation energy of creep, R is the gas constant (8.31447 J mol^{-1} K^{-1}), and T is temperature. Strain rates are bracketed by 10^{-14} and 10^{-20} s^{-1} for all calculations. The faster strain rate of 10^{-14} s^{-1} represents active deformation, such as at orogenic belts (Pfiffner and Ramsay, 1982). The slower strain rate of 10^{-20} s^{-1} represents deformation on one-plate, stagnant-lid bodies, such as Mercury (Crane and Klimczak, 2017), which is one to two orders of magnitude slower than the strain rate at intraplate continental tectonic settings (Gordon, 1998). For creep parameters, we take the widely used properties of Maryland diabase (n = 3, A = 6.3x10^{-2} MPa^{-n}s^{-1}, Q = 276 kJ mol^{-1}) for the crust (Caristan, 1982), and dry olivine (n = 3, A = 1x10^{4} MPa^{-n}s^{-1}, Q = 510 kJ mol^{-1}) for the mantle (Goetze and Evans, 1979). We apply the simulated thermal evolution from Fu et al. (2014), which considered three time steps for each of their two end-member models: one with no megaregolith and one with a megaregolith layer that is 5-km thick.

We calculated the possible lithospheric structures of Vesta (Figure 8) for the end-member cases of no megaregolith (top row) and with megaregolith layer (bottom row) at different times in Vesta's thermal evolution (Fu et al., 2014). The ages refer to the time after the cessation of convection, which has been estimated to be shortly (<10 Ma) after asteroid accretion (Sterenborg and Crowley, 2013). All strength envelopes are plotted for the crust and mantle with a total thickness of 154 km. Strength in the core is not calculated because thermal structure and other necessary material properties are unknown. Any brittle behavior in the core, if present, especially with present thermal conditions, should mimic the shape of the curve of the reference state of stress (Figure 6c). All envelopes depict the strength for a lithosphere undergoing extension and shortening, showing the difference between tectonic and reference state of stress.

These results indicate that Vesta's crust and its upper mantle to ~100 km depth are entirely brittle for every combination of the parameter space. In contrast, Vesta's lower mantle is in the ductile regime only early in its history and only in the lower range of considered strain rates. For the case without megaregolith, the brittle–ductile transition (BDT) occurs at a depth of ~85 km at 20−100 Ma (Figure 8a). At 500 Ma, the BDT migrated deeper to depths of ~110 km for the lower strain rate and ~140 km for the higher strain rate. (Figure 8b). At present, crust and mantle are completely brittle for the considered strain rates (Figure 8c). For the case with megaregolith, this 5-km layer slows the cooling process of the asteroid. In Vesta's early history, the strength envelopes with insulating megaregolith layer (Figure 8d) are nearly indistinguishable from the one without regolith (Figure 8a), but the lower mantle remains in the ductile regime for much longer, potentially until 1500 Ma after accretion for the slow strain rates, while the crust and mantle would have been entirely brittle for fast strain rates at that point in time (Figure 8e). Crust and mantle are brittle for both strain rates at present (Figure 8f). In addition, the brittle upper portion of the lithosphere will be even thicker than depicted in Figure 8 for even higher strain rates, such as would be expected during an impact.

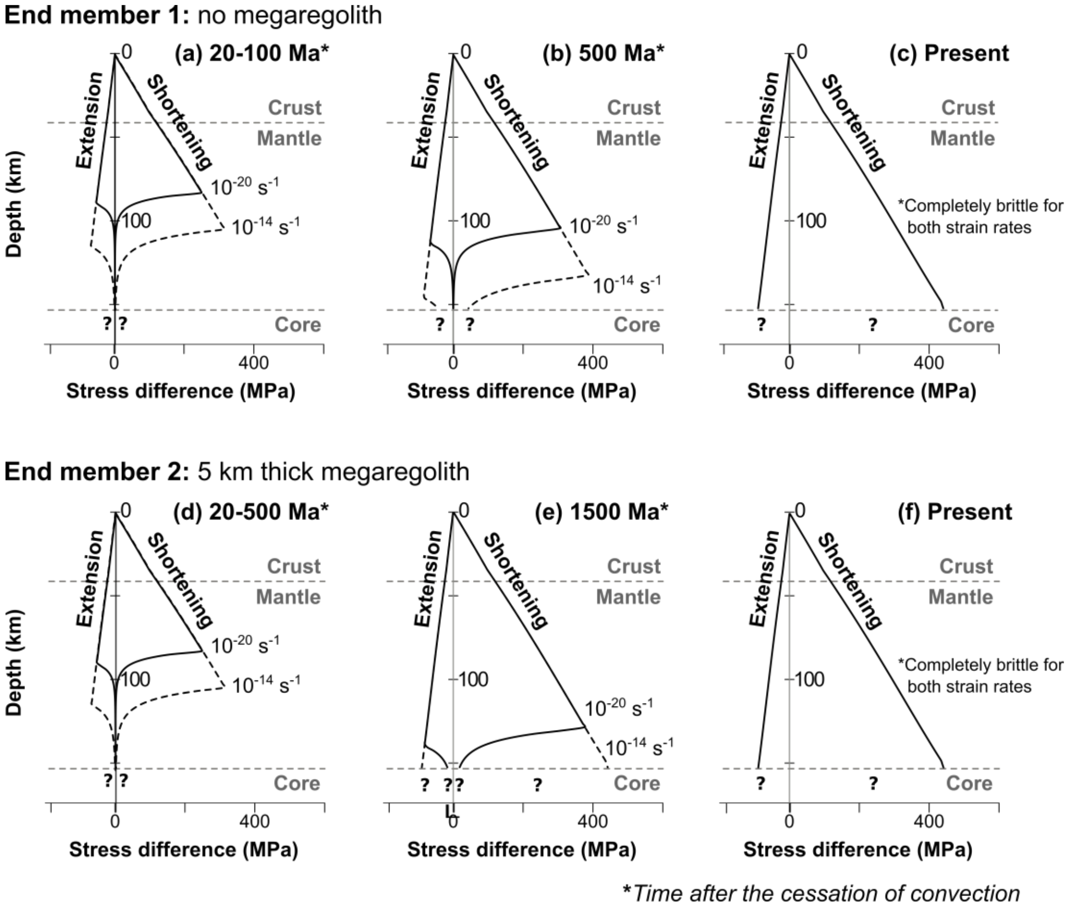

Figure 8. *Strength envelopes and evolution for lithospheres under extension and shortening calculated for scenarios where Vesta has no megaregolith (top row) or with 5 km thick megaregolith (bottom row). Lithospheric structures with no megaregolith at (a) 20−100 Ma after the cessation of accretion, estimated to be <10 Ma after asteroid accretion, (b) 500 Ma., and (c) present. Lithospheric structures with insulating megaregolith at (d) 20−500 Ma, (e) 1500 Ma, and (f) present. The time steps and end-members are based on the thermal evolution simulated by Fu et al. (2014). <1.5 column, black and white>*

4.3. Depth extent of frictional sliding

These results establish that Vesta's lithosphere is thick and that the crust and much of the mantle were in the brittle regime throughout Vesta's history for every combination of plausible parameters. The deformation behavior in the upper ~100 km of the lithosphere can thus be further assessed with more complex brittle failure criteria. Specifically, we employ the Coulomb criterion (Handin, 1969; Schofield, 2005) to assess the depth at which frictional sliding is predicted in Vesta's lithosphere. The Coulomb criterion is better suited than Byerlee's law for the tectonics of Vesta, because it relates loading conditions to frictional and cohesive properties of the rock volume, whereas Byerlee's law assumes no cohesive strength (e.g., rubble pile conditions) at the surface of the lithosphere (Schultz, 1992). Vesta is likely a monolithic, albeit highly fractured asteroid, as a prominent slumping block at Matronalia Rupes indicates that Vesta's lithosphere has some cohesive strength (Krohn et al., 2014). Furthermore, mass wasting structures on Vesta maintain most of their original shape along the surface of rupture, indicating that cohesion within the sliding mass prevents extensive spreading (Otto et al., 2013). No observation of Vesta suggests it is a cohesionless rubble pile asteroid. Hence, we consider Vesta to have a lithosphere consisting of a fractured basaltic rock mass possessing some strength at the surface that is best characterized with the Coulomb criterion.

Principal stresses in a dry lithosphere for the Coulomb criterion for frictional slip (Jaeger et al., 2007, p. 92) are given as:

$$\sigma_1 = \sigma_c + \sigma_3(\sqrt{\mu^2 + 1} + \mu)^2, \qquad (6)$$

where σ_c represents the unconfined compressive strength of intact rock and μ the coefficient of friction. By this relationship, unconfined compressive strength is a measure of the cohesive properties of the rock, and it closely relates to the cohesion term in the form of the Coulomb criterion in Mohr space. As Vesta's lithosphere has likely never been intact, the unconfined compressive strength must be adjusted for rock mass conditions (see below). For the coefficient of friction, values of $\mu = 0.85$ and $\mu = 0.6$ are used for the pressures below and above 110 MPa, consistent with Byerlee's intermediate and high friction laws (Byerlee, 1978). Vesta's crust and most of its mantle fall under intermediate pressure friction law as 110 MPa is not reached until the lowermost mantle at ~146 km (Figure 7c).

Values of unconfined compressive strengths from rock testing of a series of intact basalt samples fall between 168 MPa and 364 MPa (Schultz, 1993, 1995). As no rock sample from Vesta has been tested for its unconfined compressive strength, we assume that intact basaltic rocks on Vesta display a similar range of compressive strengths at unconfined conditions (i.e., at the surface). Because Vesta's lithosphere is not expected to be intact, these values of unconfined compressive strength for intact rock must be adjusted for rock-mass conditions.

A rock mass consists of small and large blocky, interlocked rock fragments, held together by the frictional properties of fractures forming the fragments, with rock-mass strength properties depending on the degree and nature of fracturing. Rock Mass Rating system (RMR) is commonly used to assess the degree and nature of fracturing of a rock mass (Bieniawski, 1989; Aksoy, 2008) and has previously been applied to a variety of topics in planetary rock mechanics (e.g., Schultz, 1993; Schultz et al., 2006; Nahm and Schultz, 2007; Klimczak, 2015). The rating ranges from 0 to 100, with 100 representing intact rock and values less than 25 corresponding to rubble-pile conditions. For reference, RMR = 75 refers to a relatively fresh, unweathered volume of strong basaltic rock with ~3 sets of widely spaced, clean, and rough joints (Schultz, 1995), leading to tightly interlocking angular blocks of rock. In contrast, RMR = 25 refers to disintegrated rock masses consisting of poorly interlocked, heavily broken rock pieces, which serves as a useful lower limit of a cohesive rock mass (pp. 119 in Schultz, 2019). Nearly all imaged asteroids have impact craters with diameters comparable to the body itself (Bottke et al., 2002). The size and age of

Vesta's craters imply that its interior must have been highly fractured since its early geologic history (Davison et al., 2013). Since Vesta is neither a cohesionless rubble pile nor an intact asteroid, we take a range of $25 \leq \text{RMR} \leq 60$ to be representative of Vesta's lithosphere.

The unconfined compressive strength of a rock mass, σ_c^*, can then be determined by (Hoek and Brown, 1980):

$$\sigma_c^* = \sigma_c \sqrt{s}, \tag{7}$$

where s relates to RMR (pp. 178 in Bieniawski, 1989; Hoek, 2007) by:

$$s = e^{\frac{RMR-100}{9}} \qquad \text{for RMR} > 25 \tag{8a}$$

and

$$s = 0 \qquad \text{for RMR} < 25. \tag{8b}$$

Although we use the framework of the Hoek–Brown criterion (e.g., Hoek and Brown, 1980; Hoek et al., 2002; Langford and Diederichs., 2015) to assess the unconfined compressive strength of a rock mass, we select the Coulomb failure criterion for frictional slip (Equation 6) for its simplicity to calculate the initiation of normal faulting. The Hoek–Brown criterion is equally applicable to address this problem, but it depends on more empirical parameters that would introduce more assumptions.

We solve for the valid solutions to the Coulomb criterion for Vesta's lithosphere under extension, where normal faults are expected to form, by calculating the minimum principal stresses (σ_3) needed such that the frictional resistance to sliding is overcome, and normal faulting is triggered. We present these solutions for the lower and upper strength limits of intact basalts adjusted for the full range of degrees of fracturing from rubble pile conditions to intact rock (i.e., $0 \leq \text{RMR} \leq 100$) over the entire depth of the brittle lithosphere as 3-dimensional curves (Figure 9).

The curves present the conditions at which frictional sliding is possible for the full range of degrees of fracturing from rubble pile conditions to intact rock with the minimum principal stresses at zero marking the transition to a fully compressive state of stress. This transition therefore represents the minimum condition to be met in extensional tectonic regimes where normal faults are formed, with the part of the curve at $0 \leq \text{RMR} \leq 25$ being analogous to Byerlee's law (as in Equation 3) and the part of the curve at RMR = 100 analogous to the Coulomb criterion of intact rock (as given in Equation 6). The graphs indicate that rock masses with a higher degree of fracturing corresponding to lower RMR values can experience frictional sliding at a shallower depth. For cohesionless rubble piles (RMR < 25), frictional sliding and thus normal faulting can be triggered anywhere in the brittle lithosphere, including at or near the surface (Figure 9). In contrast, for an intact lithosphere (RMR = 100), conditions for frictional sliding are not met anywhere in Vesta's lithospheric crust and mantle (Figure 9).

But since Vesta's lithosphere is neither a rubble pile nor intact, we focus on the range of a highly fractured rock mass at $25 \leq \text{RMR} \leq 60$ (Figure 9). For basalts with the lower bound of strength parameters (i.e., $\sigma_c = 168$ MPa), the minimum depth at which the frictional resistance to sliding could be overcome in Vesta's lithosphere is at 3 km, but it may be as deep as 25 km, depending on the degree of lithospheric fracturing (Figure 9a). For basalts with the upper bounds of strength parameters (i.e., $\sigma_c = 364$ MPa), the minimum depth at which frictional resistance to sliding is overcome is at 5 km, but it may be as deep as 55 km for moderate degrees of fracturing (Figure 9b). These results establish that stress magnitudes needed to overcome the frictional resistance to sliding to trigger shear displacement, and thus normal faulting, are not met in Vesta's lithosphere until substantial depths of at least 3 km but as much as 55 km. Normal fault growth is therefore not predicted by the Coulomb criterion to be triggered in the uppermost 3 to 55 km of Vesta's lithosphere.

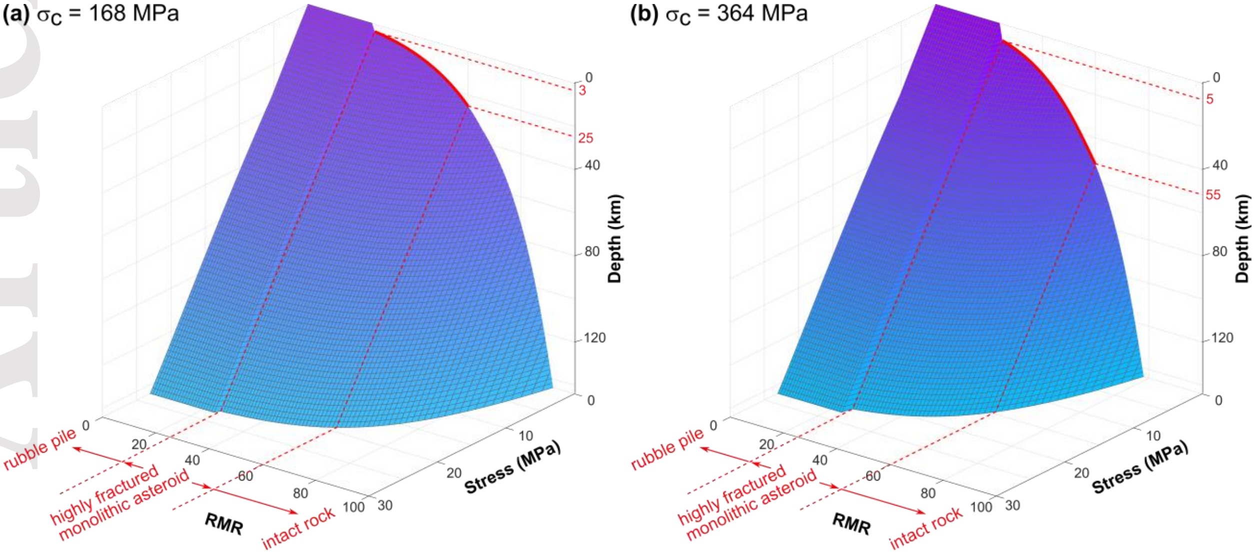

Figure 9. Valid solutions to the Coulomb criterion for lithospheric conditions of Vesta in the extensional tectonic regime calculated for basalts with unconfined compressive strengths of σ_c = 168 MPa (a) and σ_c = 364 MPa (b) that are adjusted for the full range of degrees of lithospheric fracturing from rubble pile conditions to intact rock (i.e., $0 \leq RMR \leq 100$). <2 columns, color>

5. Discussion

We investigated map patterns and the geomorphology of the large-scale troughs on Vesta, as well as the lithospheric strength to assess what type of fracture could have formed these troughs. Map patterns, geomorphology, and rock mechanical assessments individually and collectively have important implications for the tectonics on Vesta.

5.1. Geological interpretations from observations

All large-scale troughs are isolated, continuous, and subparallel among their own sets, and these lack the diagnostic map patterns of faulting or jointing. Rims of troughs are scalloped (Figure 3a), and most troughs have bowl-shaped cross-sectional geometries (Figure 4, supporting information). In contrast to previous studies (Buczkowski et al., 2012; Schäfer et al., 2014; Scully et al., 2014; Yingst et al., 2014), a distinct flat floor is not the most common trough geomorphology . A flat-floor geometry is preserved over billions of years on some terrestrial bodies, such as on the Moon (Figure 4b; Lucchitta and Watkins, 1978), Mars (Figure 4c; Kneissl et al., 2015; Ruj et al., 2019), or Mercury (Klimczak et al., 2013; Cunje and Ghent, 2016). Considering the trough geometry of a graben- or joint-origin could be degraded into a bowl shape by impact shaking and mass wasting, these findings show only that the troughs are heavily degraded, and there is no diagnostic evidence for fault traces of graben or joint walls.

Although mapping does not reveal patterns diagnostic of faulting or jointing, pit-crater chains associated with the troughs may have more definitive patterns that can be related to the origin of troughs. For example, one trough shows a direct transition to a pit-crater chain. The trough narrows toward its tips and directly transitions into a pit-crater chain, which aligns with smaller pits beyond the end of the trough (Figure 3a). Another well-preserved pit chain has larger pits in the center and smaller pits at the ends of the chain (Figure 3b). These patterns are also associated with dilational normal faults that bound grabens on Mars (e.g., Tanaka and Golombek, 1989; Montési, 2001; Wyrick et al., 2004). Some pit crater chains have larger pits in the center of the chain and smaller pits at the ends, representing different stages of fault-related landform formation (Wyrick et al., 2004). However, Martian pits are commonly located on the floors of grabens (Wyrick et al., 2004), which does not occur on Vesta. An opening-mode fracture origin may explain the absence of fault-bordered pits. Additionally, the pit craters are circular depressions that form by the collapse of material into subsurface voids, which may represent subsurface fractures that did not propagate to the surface. In this case, the preserved pit crater chain with larger pits in the center of the chain and smaller pits at the end (Figure 3b) is consistent with joints, in that the maximum aperture commonly lies at the center of the joint with smaller apertures near the tips (e.g., Vermilye and Scholz, 1995). As pit crater chains are commonly associated with grabens or joints, their presence on Vesta does not distinguish between the two structure types.

Relief and width measurements of the troughs have implications for the graben and opening-mode fracture interpretations by relating them to the corresponding structural components. Vesta is a small body that is not in hydrostatic equilibrium, its lithosphere is thick relative to the size of the body, and its troughs are long enough to encircle two-thirds of its equator. Planetary curvature in elastic interactions may make interpretations of displacements and their distributions difficult. However, this effect is difficult to quantify, given the irregular shape of the asteroid.

Nevertheless, trough reliefs were previously measured as permanent deformation in the form of vertical displacements of graben components (Buczkowski et al., 2012). We followed these authors' methods and collected measurements of elevation differences between the trough floor and rims along the trough length. Relief profiles do not reach a maximum near the midpoint of a trough and taper toward the trough tips. Moreover, the point of maximum relief is located at different locations along the bounding scarps of every structure investigated (Figure 5). Following observations of the mechanics of fault growth (e.g., Dawers et al., 1993; Cartwright et al., 1996), these observations imply that the proposed faults originated at different positions but grew toward one another to interact and form grabens. However, none of the patterns indicating fault interaction, such as segmentation and linkage, are present on Vesta. Such fault growth and mismatch in locations of maximum displacements are atypical for graben.

Since the troughs are heavily degraded, the measured relief at each location may not reflect the original displacement on a fault. However, visual inspection of the troughs shows that the degree of degradation of the scarps is similar along the length of the troughs, suggesting that present-day relief corresponds to original relief, allowing at least qualitative insight into whether relief is related to fault displacement. Nonetheless, variations of relief along the troughs are inconsistent with normal fault displacement, and thus they cannot be used as evidence to support a graben origin. Hence, relief should not be regarded as a measure of vertical displacements of normal faults, nor should relief be used for fault analysis.

Trough widths may serve as a measure for apertures of opening-mode fractures. For three out of four mapped troughs at Divalia Fossae, maximum width occurs at a similar position along the trough set (Figure 6), and the cumulative width distribution is roughly symmetrical with one maximum at the center of the overall length trace, tapering toward the tips. These characteristics are consistent with opening-mode fracture mechanics, where the displacement profiles have centrally located displacement maxima that taper to zero at the fracture tips for individual joints (e.g., Vermilye and Scholz, 1995). The cumulative profiles also suggest that troughs in each set belong to a single group that formed during the same opening event, and thus troughs may be part of a large set of parallel joints. As troughs are heavily degraded, the present-day widths do not represent the widths of the original structure, and these width measurements therefore likely do not represent the actual aperture of joints. However, the degree of degradation is similar along the length of the troughs, so variations in present-day trough width may still correlate with original joint aperture.

5.2. Lithospheric fracturing behavior of Vesta

The calculated lithospheric strength shows that Vesta's crust and upper mantle are completely brittle for every combination of plausible parameters applicable to the asteroid. The Coulomb criterion predicts that in an extensional tectonic regime on Vesta, shear displacement to form normal faults by overcoming the frictional resistance to sliding is initiated only at substantial depth. Only at these depths does the prevalent pressure gradient (Figure 7c) shift all principal stress components to be compressive, such that it is possible to initiate normal faulting. For the weakest, most heavily fractured cohesive basaltic rock mass applicable to the lithosphere of Vesta, sliding-mode fracturing is predicted to be triggered no shallower than 3 km. For stronger, moderately fractured rock masses, frictional sliding and thus normal faulting is not possible to be triggered above a depth of 55 km (Figure 9). These depths are explained by the combined effect of the low gravitational acceleration and the unconfined compressive strength of a basaltic rock mass. This result is consistent with the expectation of Stickle et al. (2015) that materials within Vesta are fractured by tensile stresses, considering the added strengthening effect of the overburden pressure. Although, one might argue that there is a thick cohesionless regolith layer on the surface of Vesta and that frictional sliding could occur within the cohesionless layer (Figure 9, for RMR ≤ 25), Vesta troughs occur where regolith is thinner than 1 km (Denevi et al., 2016). Given the large size of the troughs, with maximum reliefs that generally exceed 2 km and locally 5 km, these structures must extend deeper into the lithosphere and be contained in fractured but cohesive basalt.

Although small graben have formed in low-cohesion regolith on the Moon, a cohesionless regolith layer need not be present for normal faulting to develop on the surface of the Moon or Mars as the effects of the 6x and 15x greater gravitational acceleration on these bodies allow frictional sliding to occur at much shallower depths. For the same basaltic strength properties, frictional sliding is predicted to occur at depths as shallow as ~0.62 km on the Moon and ~0.27 km on Mars. In contrast, large-scale fracturing on other monolithic, low-gravity bodies, such as 2 Pallas, 10 Hygiea, and 16 Psyche or perhaps even Phobos, may also be driven mainly by jointing. Because Phobos is not a rubble pile but a very small, cohesive body, faulting is not expected, and its grooves probably formed through opening-mode displacements.

Owing to the strength of basaltic rock masses and the low gravity of Vesta, normal faulting is not required to explain the troughs. Even if normal faulting occurred at depth, it must have been preceded or accompanied by large opening-mode fractures above depths where normal faulting is possible. At shallower depths, the prevalent pressure gradient on Vesta is not steep enough to have placed the lithosphere experiencing extension into a fully compressive stress state, instead of requiring tensile stresses there. Opening-mode fracturing, such as jointing, is the preferred fracturing mode if at least one principal stress is tensile. These strength calculations do not include the effect of centrifugal acceleration that results from Vesta’s fast rotation. Because centrifugal acceleration counters the overburden pressure, incorporating centrifugal acceleration would increase the depth of the jointing–faulting transition in the equatorial region where the Divalia Fossae are located.

Large fracture openings in extensional tectonic regimes also occur on Earth. One analogue on Earth is the Almannagjá normal fault, which forms the western boundary of the Þingvellir Graben in the Reykjaneshryggur–Langjökull rift system of southwest Iceland. The fault is accompanied by joints, or fissures, which opened by as much as 60 m before the fractures were large and deep enough for them to be reactivated as normal faults, which generated a vertical displacement of 40 m (Gudmundsson, 1992, 2011). The troughs on Vesta may seem to be too large for joints as we know them on Earth. However, the scale of jointing depends not only on the strength properties of basaltic rock masses but also on gravitational acceleration that, in turn, affects the pressure gradient. Because this pressure gradient is much lower on Vesta, it is possible that joints on Vesta could be much larger than joints on Earth.

An opening-mode fracture origin of troughs

These observations of Vesta's troughs are inconsistent with normal faulting, or they are inconclusive. In contrast, none of the geology is inconsistent with jointing, and some observations support it. In particular, relief and overall shape of troughs are inconsistent with a graben interpretation, but their variations in width are consistent with a joint interpretation. Furthermore, rock-mechanical calculations suggest that initiation of faulting via frictional sliding is possible only at depths below at least 3 km, and it may not occur down to as much as 55 km, with jointing being the favorable fracturing behavior above those depths.

We propose that Vesta's large-scale troughs are the topographic expression of opening-mode displacement caused by jointing or mixed-mode fracturing that was subject to subsequent landform degradation (Figure 10). Given an extensional tectonic regime, joints on Vesta may have formed at the surface or in the subsurface (Figure 10a), regardless of their underlying cause of extension. It is beyond the scope of this manuscript to identify the actual cause of this extension. If joints propagated deep enough, exceeding the jointing-faulting transition, they may have been reactivated as normal faults at that depth, forming mixed-mode fractures. In this case, the width of the trough would consist of the joint aperture coupled with a dilational component from normal faulting. Alternatively, fractures could have formed initially beneath the jointing–faulting transition as normal faults deeper than 3 km and potentially as deep as 55 km, but it remains to be tested if the width and spacing of troughs is compatible with geologically plausible fault geometries at those depths.

During degradation of the troughs, the slope material on the wall of the scarps collapsed into the trough, widening the initially sharp and narrow V shape of the troughs and also forming the scalloped rims (Figure 10b). Collapse above subsurface openings formed pit crater chains (Figure 10b). Over time, slumping and degradation caused by slope failure and impact shaking likely further widened the troughs and caused pit crater chains to coalesce into linear troughs (Figure 10c). This process produced a variety of trough geometries, including ones that are bowl-shaped (*n*=176), flat-floored (*n*=53), or V-shaped (*n*=31), irrespective of whether the joint or mixed-mode fracture was initially formed at the surface or subsurface (Figure 10a). While normal faulting may have played a role in the formation of these troughs, we propose that trough geomorphology is governed primarily by opening-mode displacement from large-scale jointing (Figure 10a).

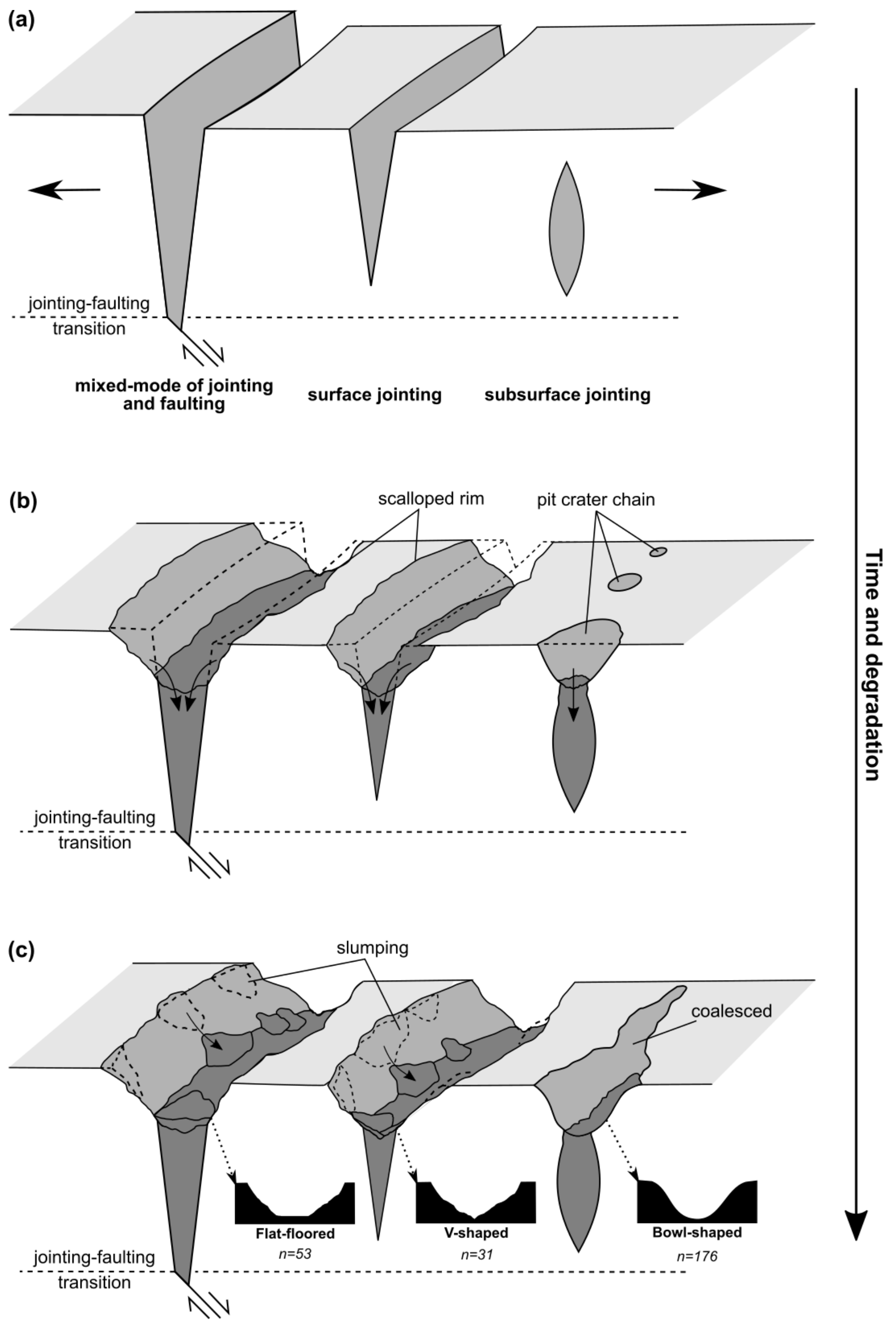

Figure 10. *Diagram showing the geomorphologic evolution for opening-mode fractures on Vesta. (a) Large-scale jointing occurs on the surface and in the subsurface. If a joint propagates deep enough, it develops into normal faulting at that depth. (b) Steep joint walls collapse into the void for the surface joints, whereas the collapse of subsurface openings forms pit crater chains. (c) Slumping and degradation widen troughs to form and coalesce the pit crater chains to form*

continuous troughs. Degradation shapes the troughs into various geometries in cross section, regardless of their origin shown in (a). The jointing–faulting transition is at least 3 km below the surface but it may be as deep as 55 km, depending on the degree of fracturing of the lithosphere. <1.5 column, black and white>

6. Conclusions

We investigated the fracture origin for the large-scale troughs on Vesta by analyzing their map patterns, cross-sectional geometries, and shape variations along the lengths of the structures. Vesta’s troughs have scalloped rims, mainly bowl-shaped and V-shaped cross-sections and points of maximum relief that are not at the midpoint of troughs. Collectively, these provide no conclusive evidence for, or are inconsistent with a graben origin. The individual and cumulative widths of troughs are instead are consistent with an origin through opening-mode fracturing.

The jointing origin is corroborated by calculations of Vesta’s lithospheric strength and fracturing behavior. Based on the end-member thermal models (Fu et al. 2014), strength envelopes suggest that Vesta’s lithospheric crust and mantle followed brittle behavior throughout much of its geologic history, considering strain rates of 10^{-20} s^{-1} and higher, applicable to an impact event with very high strain rates or to long-term planetary processes (e.g., deformation on one-plate, stagnant-lid bodies) with low strain rates. Using the Coulomb criterion for the brittle lithosphere under extension predicts that even for highly fractured basaltic rock masses, frictional sliding and thus normal faulting could be triggered only below depths of 3 km, possibly only below depths of up to 55 km, whereas jointing was consistently possible above that depth. While normal faulting could take part in the formation of these troughs at depth, the topographic expressions of the troughs are controlled primarily by opening-mode displacement from jointing. We therefore conclude that the relief of troughs was not primarily produced by faulting and should not be considered as vertical displacement on the fault. Taken together with the trough origin may not be a direct consequence of a large impact (Cheng and Klimczak, 2022), future modeling studies need to consider that the Divalia Fossae are joints or mixed-mode fractures that are resulted from a long-term tectonic consequence of the Rheasilvia impact.

While this study provides an explanation for the type of structure involved in the formation of the troughs by comparing the two plausible options of normal faulting and opening-mode fracturing, some details remain uncertain. For example, future studies should investigate the extent to which other opening-mode processes such as dike intrusions or perhaps even non-tectonic processes that served to degrade the troughs played a role in the formation and evolution of troughs. These findings and the proposed evolution of large-scale joints are important for understanding the tectonic history of Vesta. They may even help identify the type and mode of formation of large fractures on other low-gravity monolithic planetary bodies.

Acknowledgments

We thank Michael Sori, Bill McKinnon, Laurent Montesi, Nancye Dawers, Chris Okubo, Laura Fattaruso, and two anonymous reviewers, who provided feedback on several earlier versions of this manuscript. We also thank Steven Holland for his language input and proofreading of the paper. The supporting information and data of this manuscript can be accessed at Cheng (2021).

We acknowledge and thank the NASA Dawn Mission, instrument teams at the Max Planck Institute, and stereo analysis team at German Aerospace Center (DLR) for the acquisition and

processing of Dawn data used in this work. Dawn data are archived in the NASA Planetary Data System. The original data used in this study are available from https://pds-smallbodies.astro.umd.edu/data_sb/missions/dawn/index.shtml.

References

Acocella, V., Korme, T., & Salvini, F. (2003). Formation of normal faults along the axial zone of the Ethiopian Rift. *Journal of Structural Geology*, *25*(4), 503–513.

Barker, M. K., Mazarico, E., Neumann, G. A., Zuber, M. T., Haruyama, J., & Smith, D. E. (2016). A new lunar digital elevation model from the Lunar Orbiter Laser Altimeter and SELENE Terrain Camera. *Icarus*, *273*, 346–355.

Bieniawski, Z. T. (1989). Engineering rock mass classifications: a complete manual for engineers and geologists in mining, civil, and petroleum engineering. *John Wiley & Sons*.

Bottke Jr, W. F., Morbidelli, A., Jedicke, R., Petit, J. M., Levison, H. F., Michel, P., & Metcalfe, T. S. (2002). Debiased orbital and absolute magnitude distribution of the near-Earth objects. *Icarus*, *156*(2), 399–433.

Bowling, T. J., Johnson, B. C., Melosh, H. J., Ivanov, B. A., O'Brien, D. P., Gaskell, R., & Marchi., S. (2013). Antipodal terrains created by the Rheasilvia basin forming impact on asteroid 4 Vesta. *Journal of Geophysical Research: Planets*, *118*(9), 1821–1834.

Brace, W. F., & Kohlstedt, D. L. (1980). Limits on lithospheric stress imposed by laboratory experiments. *Journal of Geophysical Research: Solid Earth*, *85*(B11), 6248–6252.

Buczkowski, D. L., Wyrick, D. Y., Iyer, K. A., Kahn, E. G., Scully, J. E. C., Nathues, A., Gaskell, R. W., Roatsch, T., Preusker, F., Schenk, P. M., & Corre, L. L. (2012). Large-scale troughs on Vesta: A signature of planetary tectonics. *Geophysical Research Letters*, *39*(18), L18205.

Burov, E. B., & Diament, M. (1992). Flexure of the continental lithosphere with multilayered rheology. *Geophysical Journal International*, *109*(2), 449–468.

Byerlee, J. D. (1978). Friction of rocks. *Pure and Applied Geophysics*, *116*, 615–626.

Caristan, Y. (1982). The transition from high temperature creep to fracture in Maryland diabase. *Journal of Geophysical Research: Solid Earth*, *87*(B8), 6781–6790.

Cartwright, J. A., Mansfield, C., & Trudgill, B. (1996). The growth of normal faults by segment linkage. *Geological Society of London Special Publication*, *99*(1), 163–177.

Cheng, H. (2021). The large-scale troughs on Asteroid 4 Vesta accommodate opening-mode displacement. *Open Science Framework*. https://doi.org/10.17605/OSF.IO/GH5R9

Cheng, H. C. J., Klimczak, C., & Fassett, C. I. (2021). Age relationships of large-scale troughs and impact basins on Vesta. *Icarus*, *366*, 114512.

Cheng, H. C .J., & Klimczak, C. (2022). Structural relationships in and around the Rheasilvia basin on Vesta. *EarthArXiv*. https://eartharxiv.org/repository/view/3209/

Crane, K. T., & Klimczak, C. (2017). Timing and rate of global contraction on Mercury. *Geophysical Research Letters*, *44*(7), 3082–3089.

Crider, J. G., & Pollard, D. D. (1998). Fault linkage: Three- dimensional mechanical interaction between echelon normal faults. *Journal of Geophysical Research: Solid Earth*, *103*(B10), 24373–24391.

Cunje, A. B., & Ghent, R. R. (2016). Caloris basin, Mercury: History of deformation from an analysis of tectonic landforms. *Icarus*, *268*, 131–144.

Davison, T. M., O'Brien, D. P., Ciesla, F. J., & Collins, G. S. (2013). The early impact histories of meteorite parent bodies. *Meteoritics & Planetary Science*, *48*(10), 1894–1918.

Dawers, N. H., Anders, M. H., & Scholz, C. H. (1993). Growth of normal faults: Displacement-length scaling. *Geology*, *21*(12), 1107–1110.

Delaney, P. T., & Pollard, D. D. (1981). *Deformation of host rocks and flow of magma during growth of minette dikes and breccia-bearing intrusions near Ship Rock, New Mexico*. U.S. Government Publishing Office.

Denevi, B. W., Beck, A. W., Coman, E. I., Thomson, B. J., Ammannito, E., Blewett, D. T., Sunshine, J. M., De Sanctis, M.C., Li, J.Y., Marchi, S., Mittlefehldt, D.W, Petro, N. E., Raymond, C. A., & Russell, C. T. (2016). Global variations in regolith properties on asteroid Vesta from Dawn's low- altitude mapping orbit. *Meteoritics & Planetary Science*, *51*(12), 2366–2386.

Dula Jr, W. F. (1991). Geometric models of listric normal faults and rollover folds. *AAPG Bulletin*, *75*(10), 1609–1625.

Ermakov, A. I., Zuber, M. T., Smith, D. E., Raymond, C. A., Balmino, G., Fu, R. R., & Ivanov, B. A. (2014). Constraints on Vesta's interior structure using gravity and shape models from the Dawn mission. *Icarus*, *240*, 146–160.

Fossen, H. (2016). Faults. In *Structural Geology* (pp. 151–188). Cambridge University Press.

Fu, R. R., Hager, B. H., Ermakov, A. I., & Zuber, M. T. (2014). Efficient early global relaxation of asteroid Vesta. *Icarus*, *240*, 133–145.

Gaskell, R.W., 2012. SPC shape and topography of Vesta from DAWN imaging data. *AAS/Division for Planetary Sciences Meeting*, *44* (abstracts), 209–03.

Goetze, C., & Evans, B. (1979). Stress and temperature in the bending lithosphere as constrained by experimental rock mechanics. *Geophysical Journal International*, *59*(3), 463–478.

Gordon, R.G. (1998). The plate tectonic approximation: Plate nonrigidity, diffuse plate boundaries, and global plate reconstructions. *Annual Review of Earth and Planetary Sciences*, *26*(1), 615–642.

Grasemann, B., Martel, S., & Passchier, C. (2005). Reverse and normal drag along a fault. *Journal of Structural Geology*, *27*(6), 999–1010.

Gudmundsson, A. (1992). Formation and growth of normal faults at the divergent plate boundary in Iceland. *Terra Nova*, *4*(4), 464–471.

Gudmundsson, A. (2011). *Rock fractures in geological processes*. Cambridge University Press.

Gwinner, K., Scholten, F., Spiegel, M., Schmidt, R., Giese, B., Oberst, J., Heipke, C., Jaumann, R., & Neukum, G. (2009). Derivation and validation of high-resolution digital terrain models from Mars Express HRSC data. *Photogrammetric Engineering & Remote Sensing*, *75*(9), 1127–1142.

Handin, J. (1969). On the Coulomb- Mohr failure criterion. *Journal of Geophysical Research*, *74*(22), 5343–5348.

Hauber, E., & Kronberg, P. (2005). The large Thaumasia graben on Mars: Is it a rift? *Journal of Geophysical Research: Planets*, *110*(E7), E07003.

Hoek, E. (1994). Strength of rock and rock masse.

Hoek, E. (2007). Practical rock engineering: RocScience.

Hoek, E., & Brown, E. T. (1997). Practical estimates of rock mass strength. *International Journal of Rock Mechanics and Mining Sciences*, *34*(8), 1165–1186.

Hoek, E., Carranza-Torres, C., & Corkum, B. (2002). Hoek–Brown failure criterion—2002 edition. *Proceedings of NARMS-Tac*, *1*(1), 267–273.

Holland, M., Urai, J. L., & Martel, S. (2006). The internal structure of fault zones in basaltic sequences. *Earth and Planetary Science Letters*, *248*(1–2), 301–315.

Jaumann, R., Williams, D. A., Buczkowski, D. L., Yingst, R. A., Preusker, F., Hiesinger, H., Schmedemann, N., Kneissl, T., Vincent, J. B., Blewett, D. T., & Buratti, B. J. (2012). Vesta's shape and morphology. *Science*, *336*(6082), 687–690.

Karimi, S., & Dombard, A. J. (2016). On the possibility of viscoelastic deformation of the large south polar craters and true polar wander on the asteroid Vesta. *Journal of Geophysical Research: Planets*, *121*(9), 1786–1797.

Klimczak, C. (2015). Limits on the brittle strength of planetary lithospheres undergoing global contraction. *Journal of Geophysical Research: Planets, 120*(12), 2135–2151.

Klimczak, C., Ernst, C. M., Byrne, P. K., Solomon, S. C., Watters, T. R., Murchie, S. L., Preusker, F., & Balcerski, J. A. (2013). Insights into the subsurface structure of the Caloris basin, Mercury, from assessments of mechanical layering and changes in long-wavelength topography. *Journal of Geophysical Research: Planets*, *118*(10), 2030–2044.

Kneissl, T., Michael, G. G., Platz, T., & Walter, S. H. G. (2015). Age determination of linear surface features using the Buffered Crater Counting approach—Case studies of the Sirenum and Fortuna Fossae graben systems on Mars. *Icarus*, *250*, 384–394.

Kohlstedt, D. L., & Mackwell, S. J. (2010). Strength and deformation of planetary lithospheres. *Planetary Tectonics*, 397–456.

Krohn, K., Jaumann, R., Otto, K., Hoogenboom, T., Wagner, R., Buczkowski, D.L., Garry, B., Williams, D.A., Yingst, R.A., Scully, J. and De Sanctis, M.C. (2014). Mass movement on Vesta at steep scarps and crater rims. *Icarus*, *244*, 120–132.

Langford, J. C., & Diederichs, M. S. (2015). Quantifying uncertainty in Hoek–Brown intact strength envelopes. *International Journal of Rock Mechanics and Mining Sciences*, *74*, 91–102.

Li, J.Y., & Mafi, J.N. (2012). Body-fixed coordinate systems for Asteroid (4) Vesta. *Planetary Data System*.

Lucchitta, B. K., & Watkins, J. A. (1978). Age of graben systems on the Moon. In *Lunar and Planetary Science Conference Proceedings*, *9*, 3459–3472.

Mackwell, S. J., Bai, Q., & Kohlstedt, D. L. (1990). Rheology of olivine and the strength of the lithosphere. *Geophysical Research Letters*, *17*(1), 9–12.

Malin, M. C., Bell, J. F., Cantor, B. A., Caplinger, M. A., Calvin, W. M., Clancy, R. T., Edgett, K. S., Edwards, L., Haberle, R. M., James, P. B., & Lee, S. W. (2007). Context camera investigation on board the Mars Reconnaissance Orbiter. *Journal of Geophysical Research: Planets*, *112*(E5), E05S04.

Mao, X., & McKinnon, W. B. (2020). Spin evolution of Ceres and Vesta due to impacts. *Meteoritics & Planetary Science, 55*(11), 2493–2518.

Medwedeff, D. A., & Krantz, R. W. (2002). Kinematic and analog modeling of 3-D extensional ramps: Observations and a new 3-D deformation model. *Journal of Structural Geology, 24*(4), 763–772.

Melosh, H. J., & Williams Jr, C. A. (1989). Mechanics of graben formation in crustal rocks: A finite element analysis. *Journal of Geophysical Research: Solid Earth*, *94*(B10), 13961–13973.

Montési, L. G. (2001). Concentric dikes on the flanks of Pavonis Mons: Implications for the evolution of Martian shield volcanoes and mantle plumes. *Special Papers-Geological Society of America*, 165–182.

Nahm, A. L., & Schultz, R. A. (2007). Outcrop- scale physical properties of Burns Formation at Meridiani Planum, Mars. *Geophysical research letters, 34*(20).

Okubo, C. H. (2010). Structural geology of Amazonian-aged layered sedimentary deposits in southwest Candor Chasma, Mars. *Icarus, 207*(1), 210–225.

Okubo, C. H., & Martel, S. J. (1998). Pit crater formation on Kilauea volcano, Hawaii. *Journal of Volcanology and Geothermal Research*, *86*(1–4), 1–18.

Olson, J. E. (2003). Sublinear scaling of fracture aperture versus length: An exception or the rule? *Journal of Geophysical Research*, *108*(B9), 2413.

Otto, K.A., Jaumann, R., Krohn, K., Matz, K.D., Preusker, F., Roatsch, T., Schenk, P., Scholten, F., Stephan, K., Raymond, C.A. & Russell, C.T. (2013). Mass- wasting features and processes in Vesta's south polar basin Rheasilvia. *Journal of Geophysical Research: Planets*, *118*(11), 2279–2294.

Peacock, D. C. P., & Sanderson, D. J. (1994). Geometry and development of relay ramps in normal fault systems. *AAPG Bulletin*, *78*(2), 147–165.

Pfiffner, O. A., & Ramsay, J. G. (1982). Constraints on geological strain rates: arguments from finite strain states of naturally deformed rocks. *Journal of Geophysical Research: Solid Earth*, *87*(B1), 311–321.

Pollard, D. D., & Aydin, A. (1988). Progress in understanding jointing over the past century. *Geological Society of America Bulletin*, *100*(8), 1181–1204.

Preusker, F., Scholten, F., Matz, K. D., Roatsch, T., Jaumann, R., Raymond, C. A., & Russell, C. T. (2014). Global shape of (4) Vesta from Dawn FC Stereo images. *Vesta in the light of Dawn: First exploration of a protoplanet in the asteroid belt*, *1773*, 2027.

Ranalli, G., & Murphy, D. C. (1987). Rheological stratification of the lithosphere. *Tectonophysics*, *132*(4), 281–295.

Reches, Z. E., & Eidelman, A. (1995). Drag along faults. *Tectonophysics*, *247*(1–4), 145–156.

Resor, P. G. (2008). Deformation associated with a continental normal fault system, western Grand Canyon, Arizona. *Geological Society of America Bulletin*, *120*(3–4), 414–430.

Roatsch, T., Kersten, E., Matz, K.D., Preusker, F., Scholten, F., Elgner, S., Schroeder, S.E., Jaumann, R., Raymond, C.A. & Russell, C.T. (2015). Dawn FC2 derived vesta global mosaics V1. 0. *NASA Planetary Data System, DAWN-A.*

Robinson, M. S., Brylow, S. M., Tschimmel, M., Humm, D., Lawrence, S. J., Thomas, P. C., Denevi, B. W., Bowman-Cisneros, E., Zerr, J., Ravine, M. A., & Caplinger, M. A. (2010). Lunar reconnaissance orbiter camera (LROC) instrument overview. *Space Science Reviews*, *150*(1–4), 81–124.

Ruesch, O., Hiesinger, H., Blewett, D. T., Williams, D. A., Buczkowski, D., Scully, J., Yingst, R. A., Roatsch, T., Preusker, F., Jaumann, R., & Russell, C. T. (2014). Geologic map of the northern hemisphere of Vesta based on Dawn Framing Camera (FC) images. *Icarus*, *244*, 41–59.

Ruj, T., Komatsu, G., Pasckert, J. H., & Dohm, J. M. (2019). Timings of early crustal activity in southern highlands of Mars: Periods of crustal stretching and shortening. *Geoscience Frontiers*, *10*(3), 1029–1037.

Russell, C. T., & Raymond, C. A. (2011). The dawn mission to Vesta and Ceres. *The Dawn Mission to Minor Planets 4 Vesta and 1 Ceres*, 3–23.

Russell, C. T., Raymond, C. A., Coradini, A., McSween, H. Y., Zuber, M. T., Nathues, A., Sanctis, M. C. D., Jaumann, R., Konopliv, A. S., Preusker, F., & Asmar, S. W. (2012). Dawn at Vesta: Testing the protoplanetary paradigm. *Science*, *336*(6082), 684–686.

Ruzicka, A., Snyder, G. A., & Taylor, L. A. (1997). Vesta as the howardite, eucrite and diogenite parent body: Implications for the size of a core and for large-scale differentiation. *Meteoritics & Planetary Science*, *32*(6), 825–840.

Schäfer, M., Nathues, A., Williams, D. A., Mittlefehldt, D. W., Corre, L. L., Buczkowski, D. L., Kneissl, T., Thangjam, G. S., Hoffmann, M., Schmedemann, N., & Schäfer, T. (2014). Imprint of the Rheasilvia impact on Vesta–Geologic mapping of quadrangles Gegania and Lucaria. *Icarus*, *244*, 60–73.

Schofield, A. N. (2005). *Disturbed soil properties and geotechnical design*. Thomas Telford.

Schultz, R. A. (1992). Limitations on the applicability of Byerlee's law and the Griffith criterion to shallow crustal conditions. *Lunar and Planetary Science Conference, 23* (abstracts),

Schultz, R. A. (1995). Limits on strength and deformation properties of jointed basaltic rock masses. *Rock Mechanics and Rock Engineering*, *28*(1), 1–15.

Schultz, R. A. (1997). Displacement-length scaling for terrestrial and Martian faults: Implications for Valles Marineris and shallow planetary grabens. *Journal of Geophysical Research: Solid Earth*, *102*(B6), 12009–12015.

Schultz, R. A. (2019). *Geologic fracture mechanics*. Cambridge University Press.

Schultz, R. A., & Lin, J. (2001). Three- dimensional normal faulting models of the Valles Marineris, Mars, and geodynamic implications. *Journal of Geophysical Research: Solid Earth, 106*(B8), 16549–16566.

Schultz, R. A., Moore, J. M., Grosfils, E. B., Tanaka, K. L., & Mege, D. (2007). The Canyonlands model for planetary grabens: Revised physical basis and implications. In M.

Chapman (Ed.), *The Geology of Mars: Evidence from Earth-Based Analogs* (pp. 371–399). Cambridge University Press.

Schultz, R. A., Okubo, C. H., & Wilkins, S. J. (2006). Displacement-length scaling relations for faults on the terrestrial planets. *Journal of Structural Geology*, *28*(12), 2182–2193.

Scully, J. E., Yin, A., Russell, C. T., Buczkowski, D. L., Williams, D. A., Blewett, D. T., Buesch, O., Hiesinger, H., Corre, L. L., Mercer, C., & Yingst, R. A. (2014). Geomorphology and structural geology of Saturnalia Fossae and adjacent structures in the northern hemisphere of Vesta. *Icarus*, *244*, 23–40.

Sierks, H., Keller, H. U., Jaumann, R., Michalik, H., Behnke, T., Bubenhagen, F., & BŘttner, I. (2011). The Dawn Framing Camera. *Space Science Reviews*, *163*, 263–327.

Smith, D. E., Zuber, M. T., Frey, H. V., Garvin, J. B., Head, J. W., Muhleman, D. O., Pettengill, G. H., Phillips, R. J., Solomon, S. C., Zwally, H. J., & Banerdt, W. B. (2001). Mars Orbiter Laser Altimeter: Experiment summary after the first year of global mapping of Mars. *Journal of Geophysical Research: Planets*, *106*(E10), 23689–23722.

Sterenborg, M. G., & Crowley, J. W. (2013). Thermal evolution of early solar system planetesimals and the possibility of sustained dynamos. *Physics of the Earth and Planetary Interiors*, *214*, 53–73.

Stickle, A. M., Schultz, P. H., & Crawford., D. A. (2015). Subsurface failure in spherical bodies: A formation scenario for linear troughs on Vesta's surface. *Icarus*, *247*, 18–34.

Tanaka, K. L., & Golombek, M. P. (1989). Martian tension fractures and the formation of grabens and collapse features at Valles Marineris. *Lunar and Planetary Science Conference Proceedings, 19,* 383–396.

Vermilye, J. M., & Scholz, C. H. (1995). Relation between vein length and aperture. *Journal of Structural Geology*, *17*(3), 423–434.

The IAU WG Cartographic Coordinates & Rotational Elements (WGCCRE) (2014). New Coordinate System for (4) Vesta.

Williams, D. A., Jaumann, R., McSween Jr, H. Y., Marchi, S., Schmedemann, N., Raymond, C. A., & Russell, C. T. (2014). The chronostratigraphy of protoplanet Vesta. *Icarus, 244*, 158–165.

Wyrick, D., Ferrill, D. A., Morris, A. P., Colton, S. L., & Sims., D. W. (2004). Distribution, morphology, and origins of Martian pit crater chains. *Journal of Geophysical Research: Planets*, *109*(E6), E06005.

Xiao, H., & Suppe, J. (1992). Origin of rollover (1). *AAPG Bulletin, 76*(4), 509–529.

Yingst, R. A., Mest, S. C., Berman, D. C., Garry, W. B., Williams, D. A., Buczkowski, D., Jaumann, R., Pieters, C. M., Sanctis, M. C. D., Frigeri, A., & Corre, L. L. (2014). Geologic mapping of Vesta. *Planetary and Space Science*, *103*, 2–23.

Zuber, M. T., McSween, H. Y., Binzel, R. P., Elkins-Tanton, L. T., Konopliv, A. S., Pieters, C. M., & Smith, D. E. (2011). Origin, internal structure and evolution of 4 Vesta. *Space Science Reviews*, *63*, 77–93.


Saturnalia Fossae
Divalia Fossae
Veneneia impact basin
Rheasilvia impact basin

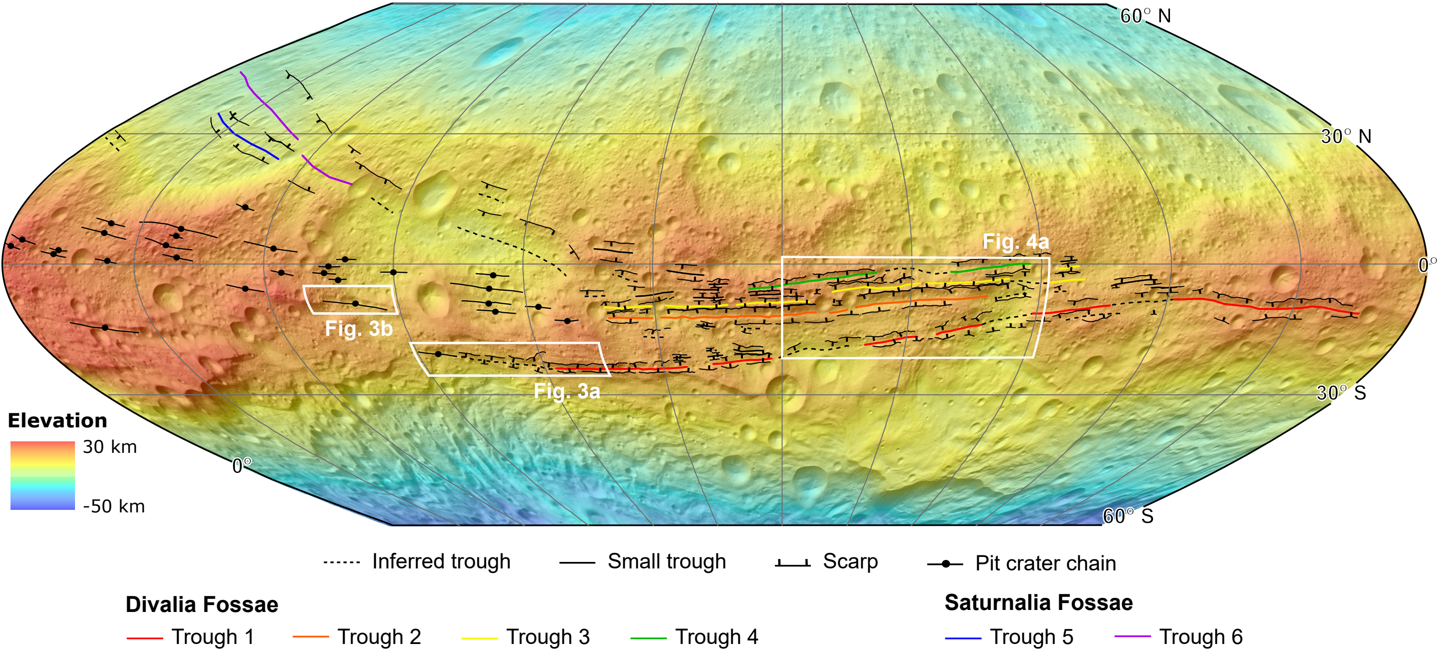
60° N
30° N
0°
30° S
60° S
0°
Fig. 4a
Fig. 3b
Fig. 3a
Elevation
30 km
-50 km
Inferred trough
Small trough
Scarp
Pit crater chain
Divalia Fossae
Trough 1
Trough 2
Trough 3
Trough 4
Saturnalia Fossae
Trough 5
Trough 6

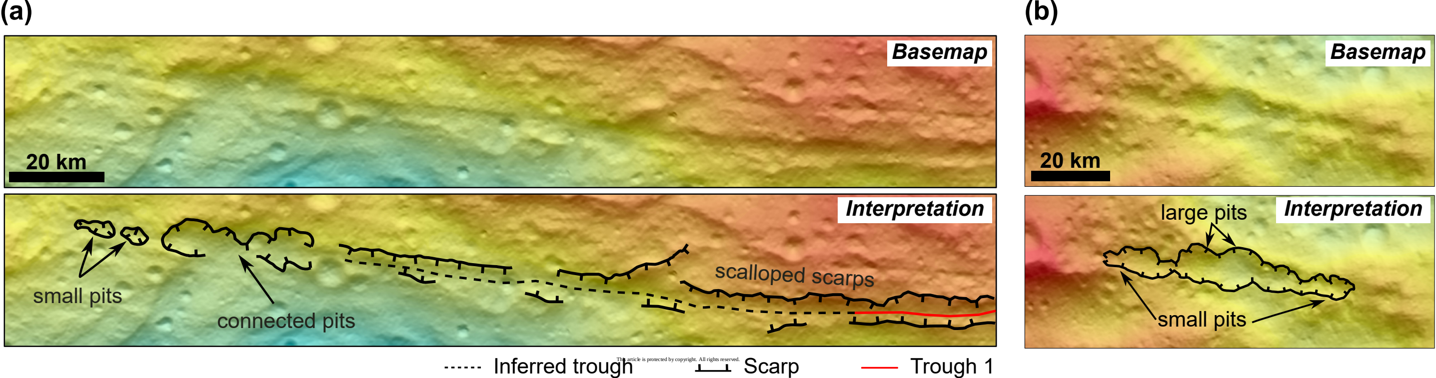
(a)
Basemap
20 km
Interpretation
small pits
connected pits
scalloped scarps
Inferred trough
Scarp
Trough 1
(b)
Basemap
20 km
Interpretation
large pits
small pits

(a) Divalia Fossae on Vesta

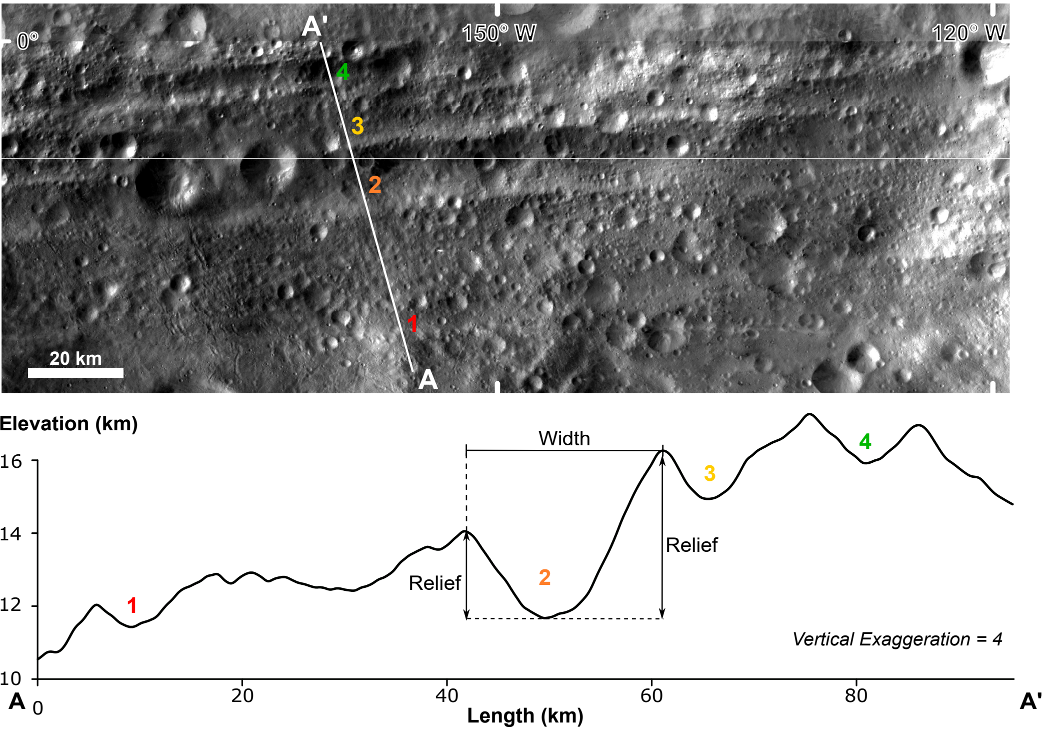

(b) Rima Ariadaeus on Moon

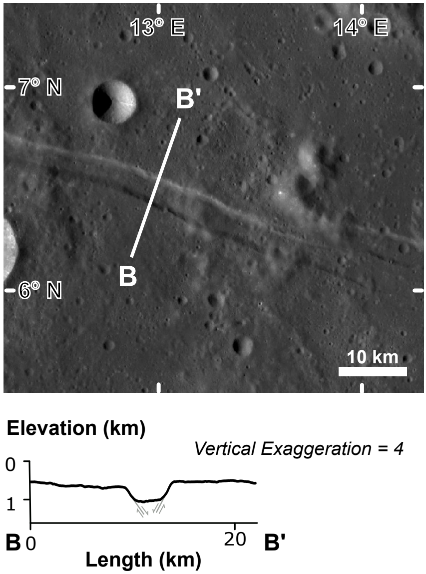

(c) Northeast flank of Alba Patera on Mars

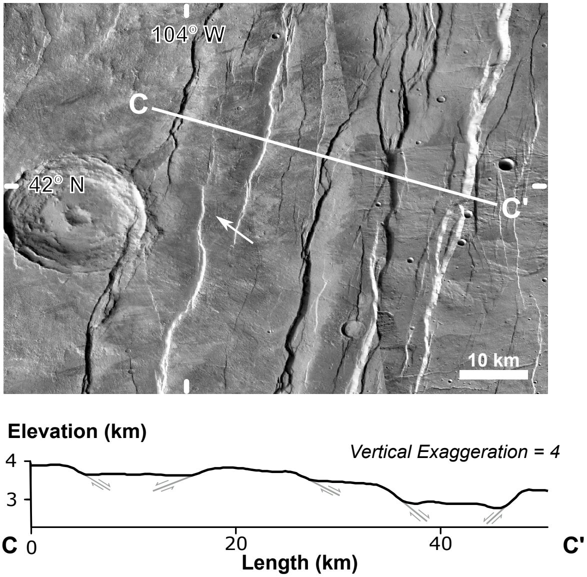

(a) Divalia Fossae

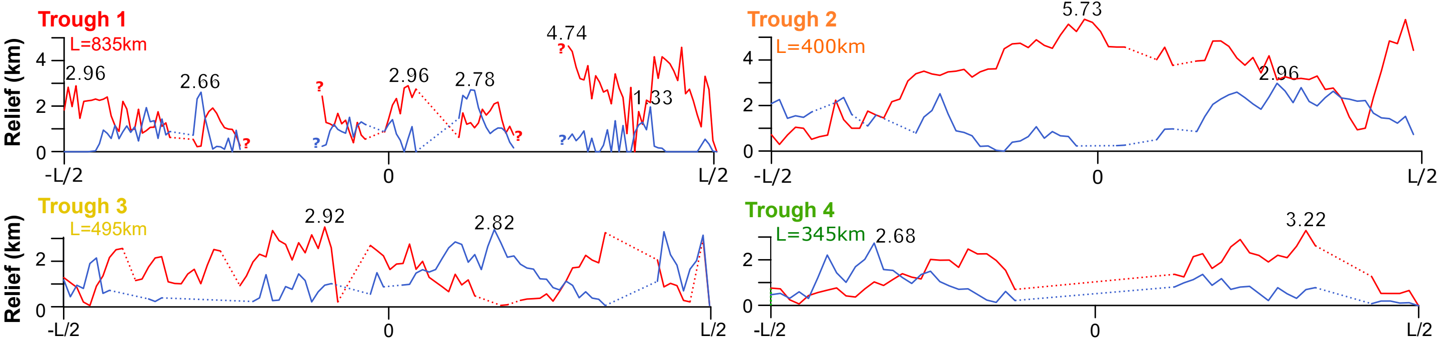

(b) Saturnalia Fossae

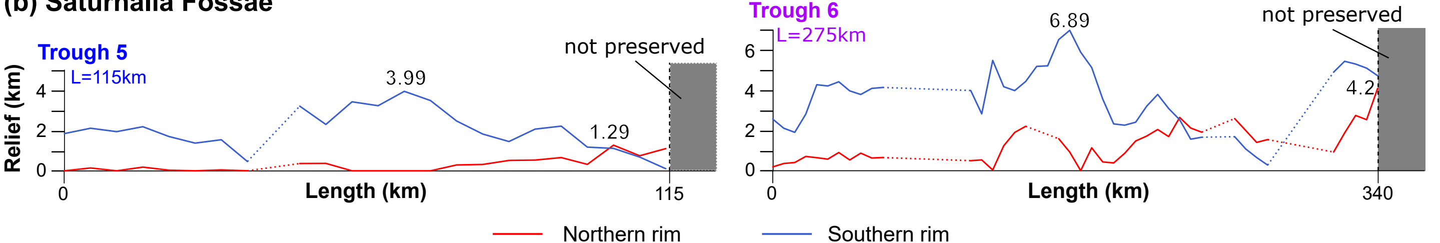

Divalia Fossae

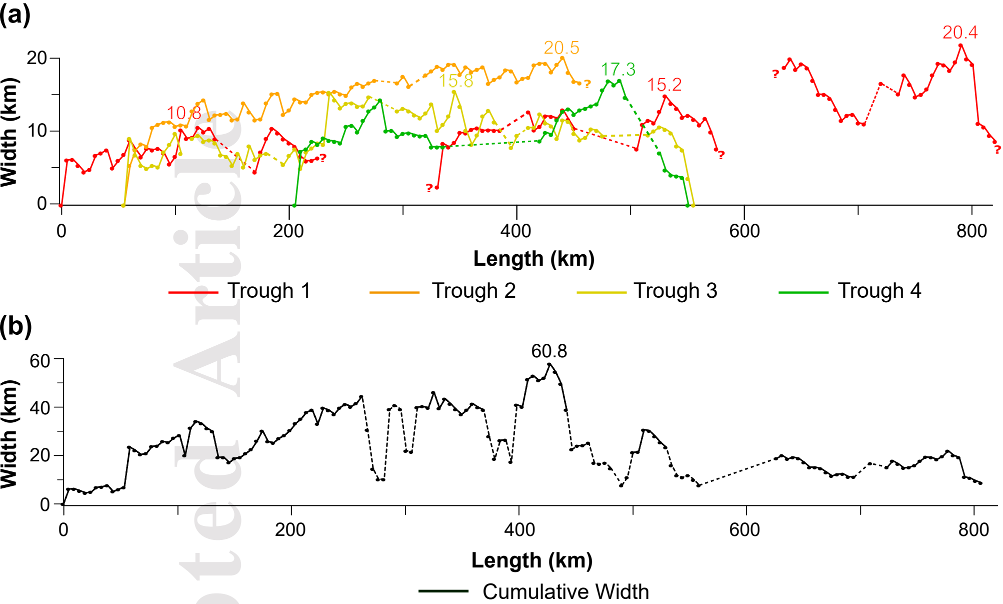

Saturnalia Fossae

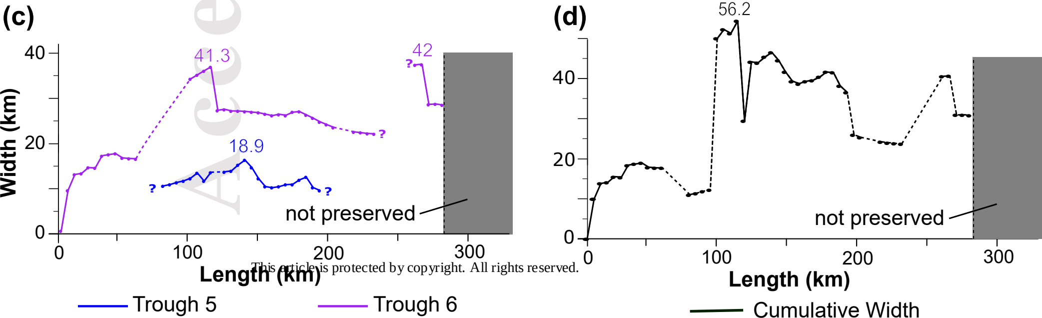

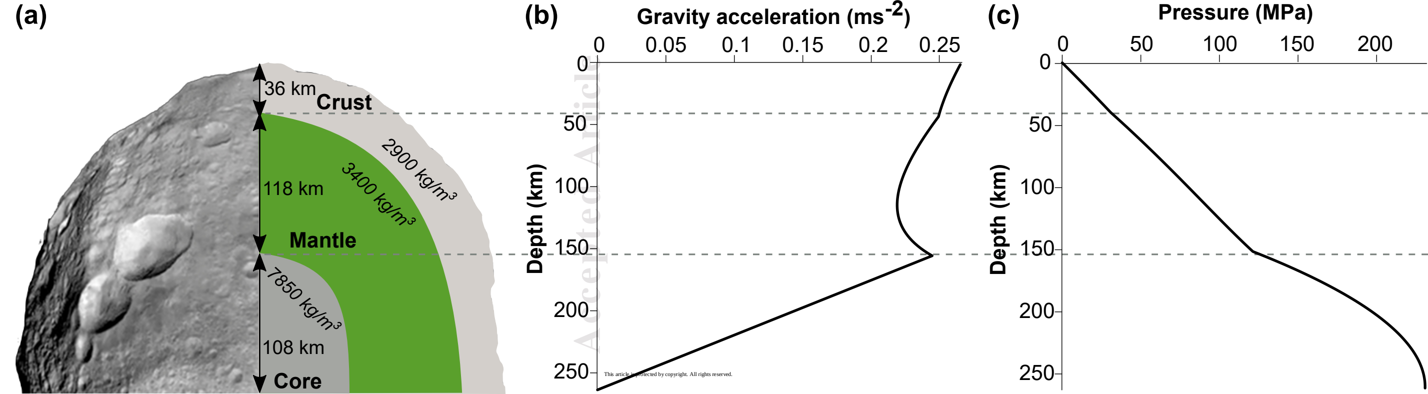
(a)
36 km
Crust
2900 kg/m³
118 km
3400 kg/m³
Mantle
7850 kg/m³
108 km
Core
(b)
Gravity acceleration (ms-2)
0
0.05
0.1
0.15
0.2
0.25
Depth (km)
0
50
100
150
200
250
(c)
Pressure (MPa)
0
50
100
150
200
Depth (km)
0
50
100
150
200
250

End member 1: no megaregolith

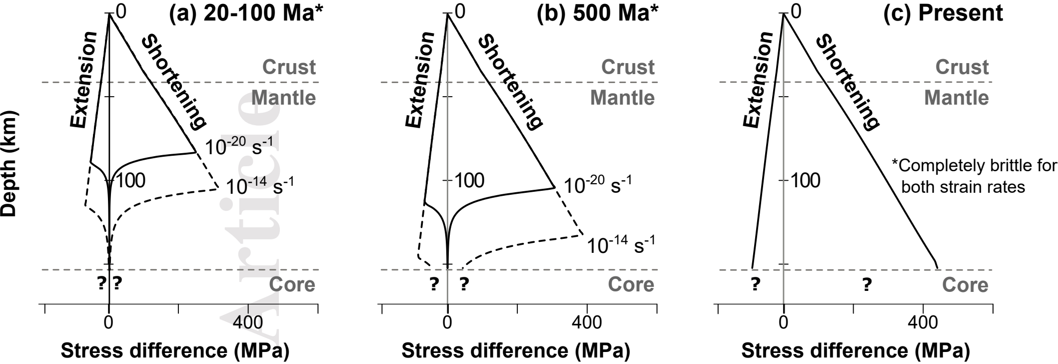

End member 2: 5 km thick megaregolith

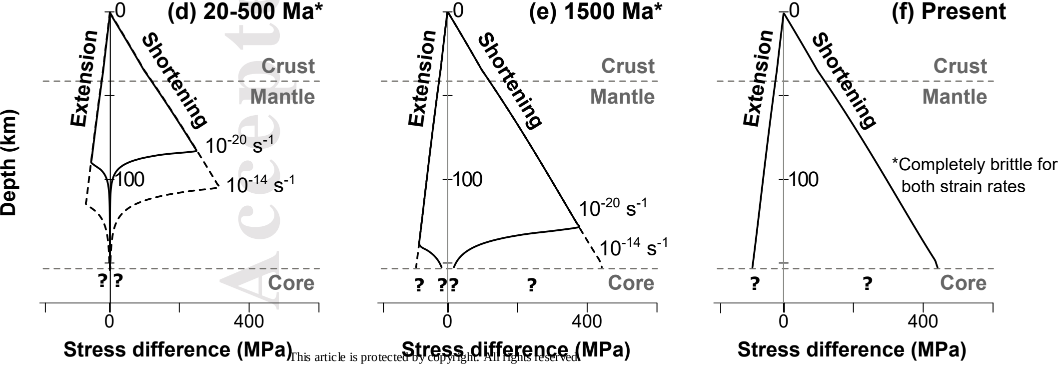

**Time after the cessation of convection*

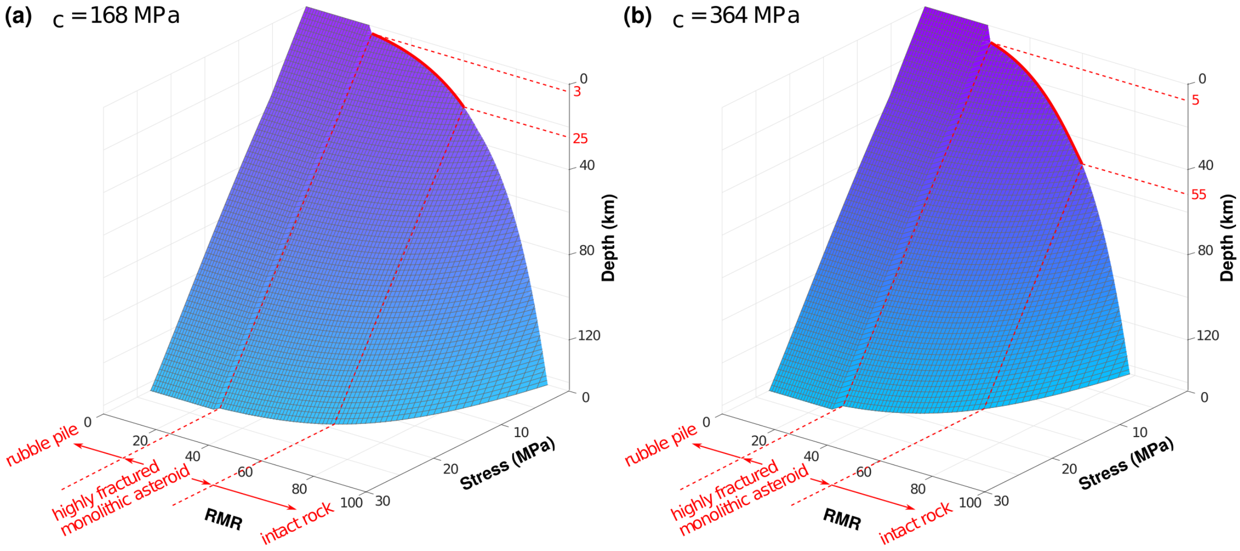
(a) c =168 MPa
0
3
25
40
80
120
0
Depth (km)
0
20
40
60
80
100
RMR
30
20
10
Stress (MPa)
rubble pile
highly fractured
monolithic asteroid
intact rock
(b) c =364 MPa
0
5
40
55
80
120
0
Depth (km)
0
20
40
60
80
100
RMR
30
20
10
Stress (MPa)
rubble pile
highly fractured
monolithic asteroid
intact rock

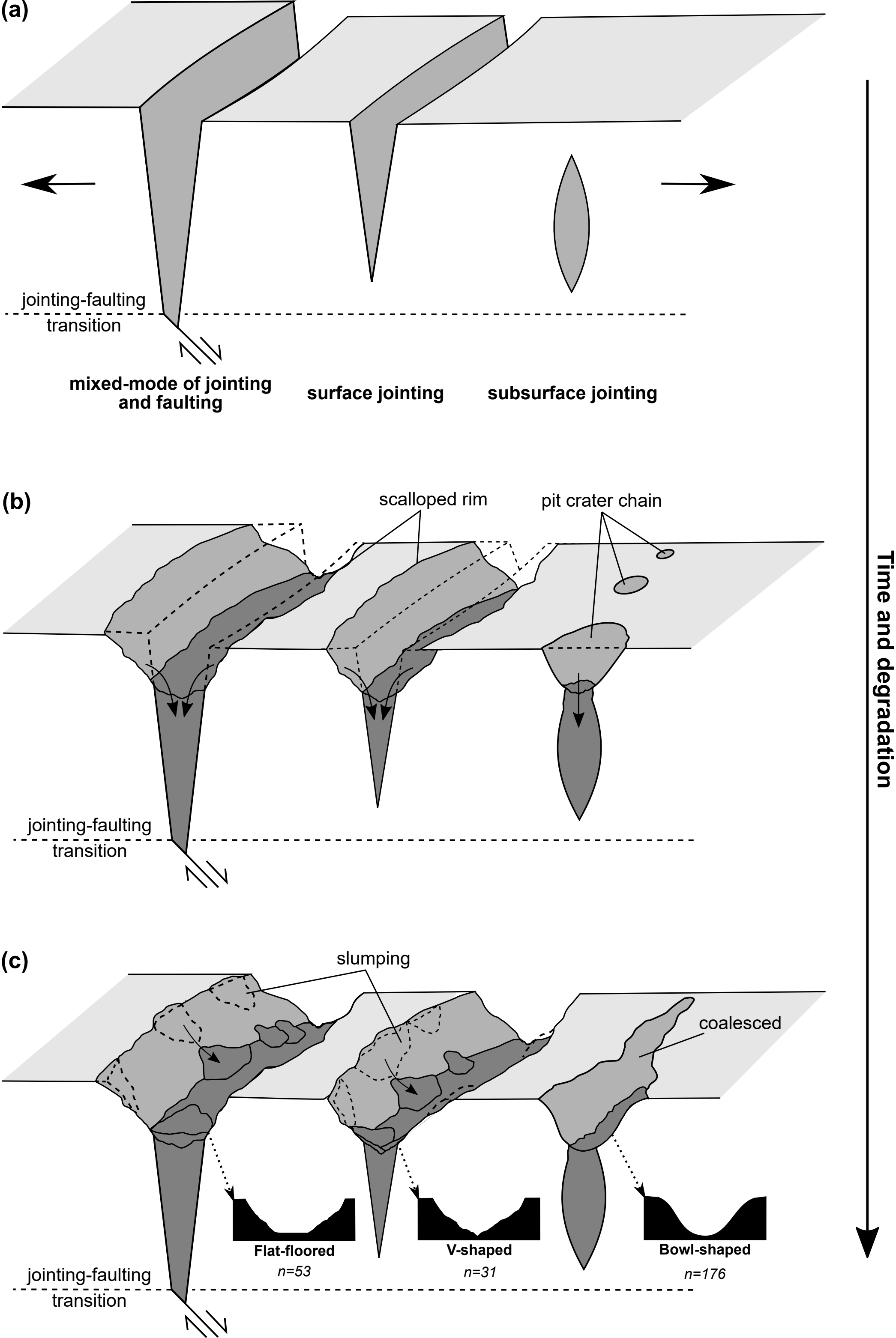
(a)
jointing-faulting transition
mixed-mode of jointing and faulting
surface jointing
subsurface jointing
(b)
scalloped rim
pit crater chain
jointing-faulting transition
(c)
slumping
coalesced
Flat-floored
n=53
V-shaped
n=31
Bowl-shaped
n=176
jointing-faulting transition
Time and degradation